OPA1 Downregulation in Skeletal Muscle Induces MERC formation in an ATF4-Dependent Manner

Antentor Hinton, Jr.,[#1,2,3,4], Prasanna Katti[#5], Margaret Mungai[1,2], Duane Hall[1,2^], Olha Koval[1,2^], Jianqiang Shao[6], Zer Vue[4], Trace A. Christensen[3], Edgar Garza Lopez[1], Rahmati Rostami[7], Kit Neikirk[4], Jacob Lam[1,2], Ahmad Alghanem[8], Jessica Ponce[1,2], Innes Hicsasmaz[1,2], Jennifer Streeter[1,2], Brandon Schickling[1,9], Serif Bacevac[1,2], Chad Grueter[1,2], Andrea Marshall[, 4], Heather K. Beasley[4], Young Do Koo[1,2], Sue Bodine[1,2], Nayeli G. Reyes Nava[10], Anita Quintana[10], Eugenia Trushina[3,11,12], Eric Weatherford[1,2], Sandra A. Murray[13], Jeffrey Salisbury[3,14], Long-Sheng Song[1,2], Isabella Grumbach[1,2], Vernat Exil[1,2], Renata O. Pereira[1,2*], Brian Glancy[5,15*], and E. Dale Abel[1,2,16*]

Affiliations:
1. Department of Internal Medicine, University of Iowa - Carver College of Medicine, Iowa City, IA, USA 52242
2. Fraternal Order of Eagles Diabetes Research Center, Iowa City, IA, USA 52242
3. Microscopy and Cell Analysis Core Facility, Mayo Clinic, Rochester, MN, USA 55905
4. Department of Molecular Physiology and Biophysics, Vanderbilt University, Nashville, TN 37232
5. National Heart, Lung, and Blood Institute, National Institutes of Health, Bethesda, MD, USA, 20892
6. Central Microscopy Research Facility, Iowa City, IA USA 52242
7. Department of Genetic Medicine, Joan & Sanford I. Weill Medical College of Cornell University, New York, NY, USA, 10065
8. King Abdullah International Medical Research Center (KAIMRC), Ali Al Arini, Ar Rimayah, Riyadh, Saudi Arabia 11481
9. Department of Medicine, Duke University, Durham, NC, USA 27708
10. Department of Biological Sciences and Border Biomedical Research Center, The University of Texas at El Paso, El Paso, TX, USA 79968
11. Department of Neurology, Mayo Clinic, Rochester, MN, USA 55905
12. Department of Pharmacology and Experimental Therapeutics, Mayo Clinic, Rochester, MN, USA 55905
13. Department of Cell Biology, School of Medicine, University of Pittsburgh, Pittsburgh, PA, 15260, USA.
14.Department of Biochemistry and Molecular Biology, Mayo Clinic, Rochester, MN, USA 55905
15. National Institute of Arthritis and Musculoskeletal and Skin Diseases, National Institutes of Health, Bethesda, MD, USA 20892
16. Department of Medicine, UCLA School of Medicine, Los Angeles, CA, USA 90095

# Authors Contributed Equally to Manuscript, co-first
^ Authors Contributed Equally to Manuscript, co-third

* co-Senior Authors

*Co-corresponding authors:

E. Dale Abel, M.D., Ph.D.

Department of Medicine

David Geffen School of Medicine and UCLA Health

757 Westwood Plaza, Suite 7236

Los Angeles, CA 90095

Phone: 310-267-3144 | Fax: 310-206-7291

Email: DOMChair_DaleAbel@mednet.ucla.edu

Brian Glancy, Ph.D.
National Heart, Lung, and Blood Institute
National Institute of Arthritis and Musculoskeletal and Skin Diseases
National Institutes of Health
10 Center Dr, Room B1D416
Bethesda MD 20892
Phone: 301-496-2679
Brian.glancy@nih.gov

Summary:

Mitochondria and endoplasmic reticulum (ER) contact sites (MERCs) are protein- and lipid-enriched hubs that mediate intracellular communications, contributing to the dynamic transfer of Ca^{2+}, lipid, and other metabolites between these organelles. Defective MERCs are associated with cellular oxidative stress, neurodegenerative disease, and cardiac and skeletal muscle pathology via mechanisms that are poorly understood. We previously demonstrated that skeletal muscle-specific knockdown (KD) of the mitochondrial fusion mediator optic atrophy 1 (OPA1) induced ER stress and upregulated Mitofusin-2, a known MERC protein. In the present study, we tested the hypothesis that *Opa1* downregulation in skeletal muscle cells induces MERC formation using multiple experimental models, including mice, *Drosophila*, and primary myotubes. Our results revealed that OPA1 deficiency increased MERC tethering and activated the integrated stress response (ISR) pathway effector, activating transcription factor 4 (ATF4). Loss of OPA1, reduced mitochondria calcium uptake and caffeine-induced calcium release by the ER, which was associated with changes in expression of mediators of calcium exchange IP_3R3, GRP75, VDAC, at MERCs. Reducing *Atf4* expression in *Opa1*-deficient muscle cells altered MERC ultrastructure changes and reestablished cytosolic calcium homeostasis. These data identify a role for ATF4 in the regulation of MERCs distance and mitochondrial calcium exchange.

Keywords: Optic atrophy 1, Mitochondria Endoplasmic Reticulum Contact, Activating Transcription Factor 4, Integrated Stress Response, Serial Block Face-Scanning Electron Microscopy, Transmission Electron Microscopy, Focus Ion Beam-Scanning Electron Microscopy,

Introduction

The endoplasmic reticulum (ER) and mitochondria continuously exchange information to sustain intracellular homeostasis, in part through physical contacts between the two organelles known as mitochondria-associated membranes (MAMs) or mitochondrial-ER contact sites (MERCs) (Rieusset, 2018). MERC dysfunction, including alterations in MERC formation and morphology, has been associated with obesity, type II diabetes (T2D), cardiovascular disease, and aging, which are disease states characterized by altered mitochondrial oxidative metabolism and insulin resistance (Rieusset, 2018).

MERC microdomains are enriched in proteins involved in mitochondrial Ca^{2+} flux, lipid transfer, and the regulation of mitochondrial (Tubbs et al., 2014, 2018). The size, density, and thickness of MERCs regulate their function, and changes in MERC distances can modulate Ca^{2+} exchange, lipid homeostasis, and cell death (Csordás et al., 2018; Delprat et al., 2019; Giacomello and Pellegrini, 2016; Hirabayashi et al., 2017; Rieusset, 2018).

Several important MERC-tethering proteins are expressed in the MERC microdomain, including Mitofusin-2 (MFN2), the inositol 1,4,5-triphosphate receptor (IP_3R3)–glucose-related protein 75 (GRP75)–voltage-dependent anion channel (VDAC) complex, the vesicle-associated membrane protein B (VAPB) and vesicle-associated membrane protein C (VAPC) complex, and others. Most known MERC proteins are located on the outer mitochondrial membrane (OMM). A relationship between the inner mitochondria membrane protein optic atrophy 1 (OPA1) and the regulation of in MERCs, was recently described (Cartes-Saavedra et al., 2022). However, a complete understanding of mechanisms linking inner mitochondria membrane proteins, OPA1

and other proteins involved in the mitochondrial cristae organizing system (MICOS), and MERC spacing, or regulation remains to be achieved.

We previously showed that *OPA1* knockdown (KD) in skeletal muscle (OPA1smko/KD) impairs mitochondrial fusion and bioenergetics, while inducing ER stress, which correlates with induction of MFN2 (Pereira et al., 2017; Tezze et al., 2017). *OPA1* KD in skeletal muscle also increases activating transcription factor (ATF4) levels (Pereira et al., 2017). Interestingly, ATF4 activation is involved in several stress processes, where ATF4 has been demonstrated to directly induce the integrated stress response (ISR) (Costa-Mattioli and Walter, 2020; Hartwick Bjorkman and Oliveira Pereira, 2021; Kasai et al., 2019; Sasaki et al., 2020). Notably, ATF4 is also linked to muscle atrophy (Pereira et al., 2017). Skeletal muscle atrophy and reduced exercise activity are associated with MERC changes (Romanello and Sandri, 2015). Age-related physical inactivity is also associated with muscle loss and reduced OPA1 levels (Tezze et al., 2017). However, the mechanisms by which ATF4 may influence the morphology of MERC microdomains in these and other contexts remain unknown.

We hypothesized that OPA1-induced mitochondrial stress increases MERCs and narrows MERC distance. To test this hypothesis, we used OPA1 loss of function in myotubes, mouse skeletal muscle, and *Drosophila* flight muscle to assess the effects of OPA1 deficiency on MERC structure. We demonstrate that OPA1 deficiency in muscle cells induces the expression of MERC proteins and increases MERC tethering. ATF4 may be required for these changes in MERC structure in OPA1-deficient muscle cells. *Atf4* loss reverses the MERC decrease driven by *Opa1* loss. Furthermore, *Atf4* overexpression was sufficient to increase MERCs formation. This increase in MERC formation may represent an initially compensatory, but ultimately

maladaptive mechanism that attempts to restore calcium homeostasis in response to OPA1-deficiency-induced mitochondrial stress.

Materials and Methods

Animal Studies

The University of Iowa Institutional Animal Care and Use Committee (IACUC) approved all protocols for animal work. For primary satellite cells isolation, 16 male mice on the C57BL/6J genetic background were used. We previously have found that male and female mice demonstrate similar effects (Pereira et al., 2017). For all gastrocnemius samples, mice were aged to 9 months. 8 control mice (*OPA1*$^{flox/flox}$) and skeletal muscle OPA1-deficient mice (*OPA1*$^{flox/flox}$ *HSA- CreER*^{T2}*)* were used to isolate primary satellite cells.

Generation of OPA1 KO animals and TUDCA treatment was achieved using protocols described by Pereira et al., 2017. The genotypes of OPA1 deficient and control mice are as described for satellite cell experiments. Standard chow was fed to mice during their 4-week recovery period following tamoxifen injections. A subgroup of OPA1 deficient and control mice were treated with TUDCA (Millipore: Billerica, MA, USA; 250 mg/kg), administered via intraperitoneal injection, Sham treated mice received equivalent volumes of phosphate-buffered saline. All animals had free access to standard chow and water, in a 22 °C environment with a 12h/12h light/dark cycle.

Primary Cell Culture

Satellite cell isolation was performed as previously described (Pereira et al., 2017). Satellite cells from *OPA1*$^{fl/fl}$ mice were plated on BD Matrigel-coated dishes and differentiated into myoblasts in Dulbecco's modified Eagle medium (DMEM)-F12 containing 20% fetal bovine serum (FBS),

40 ng/ml basic fibroblast growth factor, 1× non-essential amino acids, 0.14 mM β-mercaptoethanol, 1× penicillin/streptomycin, and Fungizone. Myoblasts were maintained with 10 ng/ml basic fibroblast growth factor and differentiated in DMEM-F12 containing 2% FBS and 1× insulin–transferrin–selenium when 90% confluency was reached. Three days after differentiation, myotubes were infected with an adenovirus expressing GFP-Cre to achieve OPA1 deletion. Adenoviruses were obtained from the University of Iowa Viral Vector Core facility. Experiments were performed between 3 and 7 days after infection.

Human Cell Culture

Human and primary mouse myotubes were grown and maintained in DMEM-F12 (Gibco, Waltham, MA, USA) supplemented with 20% fetal bovine serum (Gibco), 10 ng/ml basic fibroblast growth factor, 1% penicillin/streptomycin, 300 µl/100 ml Fungizone, 1% non-essential amino acids, and 1 mM beta-mercaptoethanol. Before plating, dishes were coated with Matrigel to enhance cell adherence. Every other day, the cells were washed with phosphate-buffered saline, and the media was replaced.

RNA Sample Preparation and Quantitative RT-PCR in Mouse Samples

RNA was isolated from 40-week-old mice. Tissue was removed from the gastrocnemius at 4 °C and immersed in TRIzol (Sigma). Total RNA was extracted in TRIzol reagent (Invitrogen) using a tissue grinder. Reverse polymerase chain reaction was performed to generate cDNA using SuperScript III (Invitrogen). For quantitative reverse transcriptase-polymerase chain reaction, 50 ng of cDNA were used for each reaction with iTAQ Universal Sybergreen (Biorad), using the QuantiStudio 6 Flex system (Applied Biosystems). Gene expression was analyzed using the $\Delta\Delta C_T$ method, and relative expression was normalized to GAPDH. Sequences for primers are listed in supplementary materials (See Table 1).

RNA Extraction and Quantitative RT-PCR for Cells

RNA extraction and quantification were performed as previously described (Pereira et al., 2017). Briefly, RNA was extracted from samples with TRIzol reagent and purified with the RNeasy kit (Qiagen Inc). The RNA was reverse transcribed, followed by qPCR reactions using SYBR Green. Samples were then loaded onto a 384-well plate, and a real-time polymerase chain reaction was performed using an ABI Prism 7900HT instrument. The primers used are listed below in Supplemental Table 1.

Western Blotting

To obtain total protein extracts from differentiated myotubes, cells were washed with ice-cold PBS before adding cold lysis buffer (25 mM Tris HCl, pH 7.9, 5 mM $MgCl_2$, 10% glycerol, 100 mM KCl, 1% NP40, 0.3 mM dithiothreitol, 5 mM sodium pyrophosphate, 1 mM sodium orthovanadate, 50 mM sodium fluoride, and protease inhibitor cocktail [Roche Applied Science: Penzberg, Germany]). Cells were scraped, homogenized with a 25-gauge needle, and centrifuged at 14,000 rpm for 10 min at 4 °C. Supernatants were collected and mixed with Laemmli sample buffer. Cell lysates were subjected to sodium dodecyl sulfate-polyacrylamide gel electrophoresis (SDS-PAGE), and proteins were transferred to nitrocellulose membranes (BioRad: Berkeley, California, USA). Membranes were blocked with 5% bovine serum albumin (BSA)-Tris-buffered saline with Tween-20 (TBST) and incubated with anti-GRP75, anti-PACS2, anti-OPA1, anti-MFN1, anti-MFN2, anti-IP_3R3, anti-VDAC, anti-BIP (GRP78), and anti-ATF-4. Quantification was performed using Image Studio Lite Ver 5.2.

Antibodies

Primary antibodies: OPA1 (1:1,000; BD Biosciences: San Jose, CA, USA; #612606), glyceraldehyde 3-phosphate dehydrogenase (GAPDH; 1:5,000; Cell Signaling Technology:

Danvers, MA, USA; #2118), MFN1 (1:1,000; Abcam, Cambridge, UK; #ab57602), MFN2 (1:1,000; Abcam; #ab101055), GRP75 (1:1000; Cell Signaling Technology; #D13H4), PACS2 (1:1,000; Abcam; #ab129402), BIP (1:5,000; BD Biosciences; #610978), ATF4 (1:1000; Proteintech; 10835-1-AP), VDAC (1:1000; Cell Signaling Technology; #4866), SERCA (1:1000; Cell Signaling Technology; #4388), MCU (1:1000; ThermoFisher Scientific; #PA5-68153), Alpha Tubulin (1:1000; Cell Signaling Technology; #2144), and IP_3R3 (1:1000; BD Biological Sciences; #610312). Secondary antibodies: IRDye 800CW anti-mouse (1:10,000; LI-COR: Lincoln, NE, USA; #925- 32212) and Alexa Fluor anti-rabbit 680 (1:10,000; Invitrogen; #A27042). Fluorescence was quantified using the LiCor Odyssey imager.

MERC Confocal Analysis

Cells were grown in culture media on a #1.5 cover glass, either embedded into a petri dish or divided with plastic-walled growth chambers, to optimize microscope optics. Cells were incubated for 30 min with MitoTracker Orange FM (Invitrogen, 400 nmol/L) and subsequently fixed in 4% paraformaldehyde to prepare for colocalization staining with GRP78. Confocal image stacks were captured with a Zeiss LSM-5, Pascal 5 Axiovert 200 microscope using LSM 5 version 3.2 image capture and analysis software and a Plan-APOCHROMAT 40x/1.4 Oil DIC objective. Images were deconvoluted with NIH ImageJ software (National Institutes of Health) and BITPLANE Imaris software. Subsequently, images were subjected to analysis using Imaris software for Mander's and Pearson's coefficient analyses. Each experiment was performed at least three times, and 10–20 cells per condition were quantified.

Sample Preparation for Transmission Electron Microscope (TEM) Analysis

Soleus muscle was freshly excised and immediately washed in ice-cold saline. Samples were processed as described by the University of Iowa Microscopy Core Facility (Pereira et al., 2017).

Mice were anesthetized with isoflurane according to prior protocols (Garza-Lopez et al., 2022; Lam et al., 2021; Neikirk et al., 2021; Vue et al., 2022).

The soleus samples were fixed with TEM fixative and stained. Random images of intermyofibrillar (IMF) sections were obtained. TEM was used to view the ultrastructure of the samples to quantify MERCs.

Cells were fixed in 2.5% glutaraldehyde in sodium cacodylate buffer for 1 hour at 37 °C, embedded in 2% agarose, postfixed in buffered 1% osmium tetroxide, stained in 2% uranyl acetate, and dehydrated with an ethanol graded series. After embedding in EMbed-812 resin, 80 nm sections were cut on an ultramicrotome and stained with 2% uranyl acetate and lead citrate. Images were acquired on a JEOL JEM-1230 Transmission Electron Microscope, operating at 120 kV.

TEM Analysis

Measurements of mitochondrial area, circularity, and length were performed using the multi-Measure region of interest (ROI) tool in ImageJ (Garza-Lopez et al., 2022; Lam et al., 2021; Neikirk et al., 2021; Parra et al., 2014; Vue et al., 2022). To measure cristae morphology, we used ROIs in ImageJ to determine the cristae area, circulatory index, number, and cristae score. Cristae volume was determined by the sum of all cristae area divided by total area of mitochondria (Patra et al., 2016). The NIH ImageJ software was used to manually trace and analyze all mitochondria or cristae using the freehand told in the ImageJ application (Parra et al., 2014). We also measured MERC distance, length, and percent coverage. MERC length was defined as the horizontal distance between the mitochondria and ER interface. MERC distance was defined as the vertical distance between the mitochondria and ER interface. MERC

percentage coverage was calculated as the total ER or mitochondrion surface area normalized to the distance between the mitochondria and the ER.

Serial Block Facing-Scanning Electron Microscopy (SBF-SEM) Processing for *Drosophila* Muscle Fibers

Tissue was fixed in 2% glutaraldehyde in 0.1 M cacodylate buffer and processed using a heavy metal protocol adapted from a previously published protocol (Courson et al., 2021; Mustafi et al., 2014). Tissue was immersed in 3% potassium ferrocyanide and 2% osmium tetroxide (1 hour at 4 °C), followed by filtered 0.1% thiocarbohydrazide (20 min), 2% osmium tetroxide (30 min), and left overnight in 1% uranyl acetate at 4 °C (several de-ionized H_2O washes were performed between each step). The next day, samples were immersed in a 0.6% lead aspartate solution (30 min at 60 °C and dehydrated in graded acetone (as described for TEM). The tissues were impregnated with epoxy TAAB 812 hard resin, embedded in fresh resin, and polymerized at 60 °C for 36–48 hours. After polymerization, the block was sectioned for TEM to identify the area of interest, then trimmed to 0.5 mm × 0.5 mm and glued to an aluminum pin. The pin was placed into an FEI/Thermo Scientific Volumescope 2 scanning electron microscope (SEM), a state-of-the-art SBF imaging system. For 3D EM reconstruction, thin (0.09 µm) serial sections, 300 to 400 per block, were obtained from the blocks that were processed for conventional TEM. Serial sections were collected onto formvar coated slot grids (Pella, Redding CA), stained, and imaged, as described above. The segmentation of SBF-SEM reconstructions was performed by manually tracing structural features through sequential slices of the micrograph block. Images were collected from 30–50 serial sections, which were then stacked, aligned, and visualized using Amira (Thermo Fisher Scientific, Waltham, Massachusetts, USA) to make videos and quantify volumetric structures (Garza-Lopez et al., 2022).

Proximity Ligation Assay in Cells

We used Duolink In Situ Detection Reagents Red (Sigma-Aldrich; DUO92008) to verify the proximity of two antibodies of interest in cell culture. Previously validated antibodies were used. The first antibody was mouse monoclonal antibody against MFN1 (Abcam #ab57602), the second antibody was a rabbit polyclonal antibody against MFN2 (Abcam #ab50843), produced using a synthetic peptide corresponding to human Mitofusin 2, aa 557–576, conjugated to keyhole limpet hemocyanin (KLH). Both antibodies were determined to work at a 1:200 dilution. Three controls were included in these experiments. Each primary antibody was omitted from separate cells to determine the non-specific binding of the primary antibodies and to confirm the optimal antibody titer. One well was devoid of all primary antibodies to detect any non-specific binding of the Duolink© PLA probes.

Cells were fixed in 4% paraformaldehyde in PBS at 37 °C for 10 minutes. After three rinses with PBS, a permeabilization solution containing 0.02% Triton X-100 in PBS was applied for 10 minutes. A ready-to-use blocking solution from the kit was applied for 1 hour at 37 °C. A cocktail containing both antibodies or a control solution, diluted in the provided diluent, was applied to the cells overnight at 4 °C. The next day, cells were washed and incubated in a pair of oligonucleotide-labeled secondary antibodies, one against mouse and one against rabbit, for 1 hour at 37 °C. Cells were washed again and hybridized with the ligase solution for 30 minutes at 37 °C, connecting the oligos in close proximity to each other and forming a closed circle DNA template. Cells were then washed, rolling circle amplification (RCA) was performed with the template, with the probe acting as a primer for the DNA polymerase. RCA was allowed to proceed in a dark hybridization chamber at 37 °C for 1 hour and 40 minutes. Then, cells were washed and mounted in Duolink mounting media and stored at 4 °C overnight and imaged with

an SP-8 confocal inverted microscope using a white laser light set to an excitation wavelength of 594 nm and an emission wavelength of 624 nm ± 10 nm.

Proximity Ligation Assay in Tissue

Duolink In Situ Detection Reagents Red (Sigma-Aldrich; DUO92008) was used to verify the proximity of two antibody locations in tissue samples. We used the two antibodies described for cells. Both antibodies were determined to work at a 1:50 dilution.

One tissue slide was devoid of both primary antibodies to detect any non-specific binding of the Duolink PLA probes. The tissues were fixed in a manner similar to the cells described above; however, tissue fixation occurred in warm 4% paraformaldehyde in PBS at 37 °C for 24 hours rather than the 10 minutes used for cells. After fixation, tissues were mounted in optimal cutting temperature (OCT) medium.

Fly Strains and Genetics

Genetic crosses were performed on yeast corn medium at 22 °C unless otherwise noted. W^{1118} were used as controls for the respective genetic backgrounds. *Mef2-Gal4* (III) was used to drive muscle-specific *Opa1-like* (Opa1). *Tub-Gal80*^{ts}; *Mef2 Gal4* (BS# 27390) was used for the conditional *Opa1-like* muscle-specific gene KD. Genetic crosses were set up at 18 °C and then shifted to 29 °C at the larval stage. *UAS-mito-GFP* (II chromosome) was used to visualize the mitochondria. Stocks were requested or obtained from the Bloomington *Drosophila* stock center. All chromosomes and gene symbols are as described in Flybase (http://flybase.org).

Mitochondrial Staining

Indirect flight muscles (IFMs) from 2–3-day-old adult flies were dissected in 4% paraformaldehyde (Sigma) and fixed in 4% paraformaldehyde for 1.5–2 hours on a rotor with a minimum rpm. Samples were washed in PBSTx (PBS +0.03% TritonX-100) three times each for

15 min and incubated in 500–1000 nM solution of Mitotracker in PBS (M22425, Molecular Probes; 1 mM stock in dimethyl sulfoxide, DMSO) at 37 °C for 30 min. *DMef2-Gal4* driven *UAS-mito-GFP* was also used to image mitochondria. Muscle samples were washed and counterstained with Phalloidin-TRITC or FITC (P1951-TRITC, Sigma-Aldrich, 50 µg/ml stock) and mounted using Prolong Glass Antifade Mountant with NucBlue (P36985, ThermoFisher, USA). Samples were imaged using a ZEISS 780 confocal microscope and processed using ZEN software (version 3.2.0.115).

Immunohistochemistry

Two-day-old adult fly thoraces were dissected to obtain IFMs in 4% paraformaldehyde (Sigma), and the muscle was fixed in 4% paraformaldehyde (Sigma) for 1.5–2 hours at 25 °C on the rotor. Samples were washed three times with PBSTx for 15 min and blocked for 2 hours at 25 °C or overnight at 4 °C using 2% BSA (Sigma). Samples were incubated with respective primary antibodies at 4 °C overnight. Later, samples were washed three times for 10 min with PBSTx and incubated for 2.5 hours in respective secondary antibodies at 25 °C or overnight at 4 °C. Samples were then incubated for 40 min with Phalloidin-TRITC (2.5 µg/ml; P1951, Sigma, USA) to counterstain samples and mounted using Prolong Glass Antifade Mountant with NucBlue stain (P36985, ThermoFisher, USA), after incubation for 20 min at 25 °C. Images were acquired using the ZEISS 780 confocal microscope and processed using ZEN software (version 3.2.0.115). Antibodies used for the staining were rabbit anti-PAC (1:20), rabbit anti-VDAC1 (1:200), rabbit anti-IP3 (1:200), and Alexa Fluor-488-labeled anti-rabbit IgG (1:500, ThermoFisher, USA).

Electron Microscopy (EM) Sample Preparation in Flies

Flies (2–3 days old) were dissected in standard fixative (2.5% glutaraldehyde, 1% paraformaldehyde, and 0.12 M sodium cacodylate buffer). Individual *Drosophila* muscle fibers (IFMs) were isolated and transferred to a fresh fixative tube. Fixation and imaging were performed as described above.

RNA Sample Preparation in Flies

RNA was isolated from the IFMs of 1–2-day-old flies. IFMs were removed from the bisected thoraces at 4 °C and immersed in TRIzol (Sigma). Total RNA was extracted in TRIzol reagent (Invitrogen) using a tissue grinder. Reverse polymerase chain reaction was performed to generate cDNA using SuperScript III (Invitrogen). For quantitative reverse transcriptase-polymerase chain reaction, 50 ng of cDNA were used for each reaction with iTAQ Universal Sybergreen (Biorad), using the QuantiStudio 6 Flex system (Applied Biosystems). Gene expression was analyzed using the $\Delta\Delta C_T$ method, and relative expression was normalized to GAPDH. Sequences for the primers are listed in supplementary materials (Table 2)

RNA-seq

RNA-seq was performed in accordance with prior protocols (Hall et al., 2017; Ponce et al., 2020). The Genomics Division of the University of Iowa Institute of Human Genetics initially isolated RNA from each of 5 WT and OPA1 KD flies. Sequences were uploaded to Kallisto. Reads were quantified using Kallisto (v0.46.2) and an index built with a fasta file of transcripts from genome assembly BDGP6.28. Differential gene expression analysis was performed using DESeq2 (v1.30.0). We assembled gene lists which revealed expression of more than 5 fragments per kilobase per million reads in either control of OPA1 KD samples and >2.0-fold change in expression. These were analyzed for biological function enrichment analysis; enriched functional classification by gene ontology analysis using Panther (http://pantherdb.org/); upstream regulator

analysis; network connectivity with Ingenuity Pathway Analysis (QIAGEN); and enriched KEGG pathways and promoter TF-binding sites using WebGestalt (http://www.webgestalt.org).

Statistical Analysis

Results are presented as the mean ± standard error of the mean. Data were analyzed using an unpaired T-test. If more than two groups were compared, one-way analysis of variance (ANOVA) was performed, and significance was assessed using Fisher's protected least significance difference test. GraphPad PRISM and Statplus software package was used for t-tests and ANOVA analyses (SAS Institute: Cary, NC, USA). For all statistical analyses, a significant difference was accepted when $P < 0.05$.

Results

Opa1-like KD in *Drosophila* Flight Muscle Alters Mitochondria, Cristae, and MERC Morphology

Mammalian OPA1 plays an essential role in mitochondrial fusion, and *OPA1* KD increases the number of fragmented mitochondria and the average number of mitochondria per cell (Cipolat et al., 2004; Frezza et al., 2006; Parra et al., 2014; Patten et al., 2014; Scorrano et al., 2002; Tezze et al., 2017; Varanita et al., 2015). We previously reported that *Opa1* downregulation in skeletal muscle of mice induces the mitochondrial fusion and MERC protein MFN2, suggesting that *Opa1* deletion may play a role in regulating MERCs. To determine the role of OPA1 in MERC formation, maintenance, and function, we analyzed the effects of *Opa1-like* KD on MERC protein expression in fly muscle tissue (Fig. 1). Expression of genes encoding ER and mitochondrial proteins, such as the mitochondrial fission protein dynamin-related protein 1 (*DRP1*) and the ER stress-related markers *ATF4*, *BIP*, and inositol-requiring enzyme 1 (*IRE1*) were increased in *Opa1-like* KD compared with wild-type (WT) *Drosophila* muscles (Fig. 1A). However, no significant difference in the ER stress marker *ATF6* expression was observed between WT and *Opa1-like* KD muscles (Fig. 1A). Transcripts encoding Ca^{2+}-related MERC components, IP_3R3 and *GRP75*, were elevated in *Opa1-like* KD fly muscle (Fig. 1A). Interestingly, the gene expression levels of the OMM protein *VDAC* (Fig. 1A) was decreased. These results indicate that *Opa1-like* KD induces the transcription of MERC components, and ER stress genes.

To examine the effects of *Opa1-like* KD on mitochondrial morphology in *Drosophila* skeletal muscle, we used confocal microscopy and transmission electron microscopy (TEM).

Confocal microscopy revealed that *Opa1-like* KD increased mitochondrial fragmentation (Fig. 1B-G), as assessed by counting the number of mitochondria in three sarcomeres (Fig. 1H). Mitochondrial area and mitochondrial aspect ratio (length:width ratio of the mitochondrial profile) were also reduced in the *Opa1-like* KD muscle (Fig. 1I-J). Similar results were obtained by TEM (Fig. 1K-N), showing that *Opa1-like* KD increased the mean circularity index, decreased the mean mitochondrial area, and increased the number of mitochondria (Fig. 1O-Q). The mitochondrial fragmentation confirms an essential role of OPA1 in mitochondrial fusion.

OPA1 deletion altered cristae morphology. We assessed the abundance and quality of cristae using the cristae score, cristae area, cristae number, and cristae volume, which were all decreased in *Opa1-like* KD mitochondria relative to control mitochondria (Fig. 1R–U). In addition, OPA1 KD was associated with loss of lamellar cristae and increased tubular cristae, supporting previous findings that OPA1 plays an important role in cristae remodeling (Cipolat et al., 2004; Frezza et al., 2006; Parra et al., 2014; Patten et al., 2014; Scorrano et al., 2002; Tezze et al., 2017; Varanita et al., 2015).

TEM was used to visualize and quantify MERC morphology in *Opa1-like* KD *Drosophila* muscle (Fig. 1V-Y). Relative to WT, *Opa1-like KD* non significantly increased contact length (Fig. 1Z), and significantly decreased the mean MERC distance (Fig. 1AA), increased the percentage of mitochondrial coverage by ER (Fig. 1AB), and increased the percentage of ER coverage by mitochondria (Fig. 1AC), suggesting that *Opa1-like* deficiency increased MERC tethering. In mammals, muscle-specific *Opa1-like* KD induced ER stress and muscle atrophy (Tezze et al., 2017). In *Opa1-like* KD flies, pupal size, fly steps per second and muscle movement were decreased and glycogen levels increased (Supplementary Figure [SF]

1A–D), (SV 1–3). Thus, *Opa1-like* KD in *Drosophila* muscle alters morphology of mitochondria and cristae, induces MERCs formation and impairs pupae development.

Loss of OPA1 Increases MERC Tethering and Protein Expression in Myotubes

We validated our *Drosophila* findings in mammalian muscle cells *in vitro* using cultured myotubes. Satellite cells were isolated from *OPA1* floxed mice. Myoblasts and differentiated myotubes were transduced with recombinant adenovirus containing the green fluorescent protein gene (Ad-GFP) or containing Cre recombinase adenovirus (Ad-CRE). The KO of *OPA1* from primary myoblasts (Fig. 2A) induced ER stress, indicated by increased BIP and ATF4 protein levels and increased levels of the MERC proteins MFN2 and GRP75 (Fig. 2B).

MFN2 may regulate MERCs (De Brito and Scorrano, 2008; Sood et al., 2014). We wanted to test if MFN2 interactions with MFN1 would be increased upon *OPA1* KO. MFN2 is normally localized to the mitochondria side of MERCs, whereas MFN1 is normally localized on the ER side. We speculated that MFN2 would colocalize to the ER side when interacting with MFN1 to form a tether. MERC interactions following *OPA1* KO were evaluated by confocal microscopy after *in situ* PLA, which showed that *OPA1* KO increased MFN2–MFN1 interactions in primary myoblasts (SV 4 and 5) and myotubes (Fig. 2C-I). ER and mitochondria colocalization in *OPA1* KO and control myoblasts and myotubes was evaluated by immunohistochemistry by determining overlap of mitotracker and GRP78 (Fig. 2J-W) using Pearson's correlation coefficient and Mander's overlap coefficient, which confirmed increased colocalization between mitochondria and ER (Figure 2X, Y, Z). MERC size increased in *OPA1* KO samples, suggesting more interactions or connections in the OPA1-deficient model (SV 12 and 13). These data suggest that OPA1 loss in primary myoblasts and myotubes increases MERC protein expression and MERC tethering.

TEM analysis (Fig. 2AA-AD) was used to investigate MERC structures with greater spatial resolution. *OPA1* KO decreased MERC distance (Fig. 2AE), increased the percentage of mitochondria surface area covered by ER (Fig. 2AF), and increased the percentage of the ER surface area covered by mitochondria (Fig. 2AG). The mitochondrial area decreased following *OPA1* KO (Fig. 2AH). Similar to *drosophila*, OPA1 deficiency in myotubes decreased the cristae number, cristae area, cristae score, and cristae volume (Fig. 2AI–2AL).

OPA1 Deficiency in Mouse Skeletal Muscle Increases MERC Sites and the Expression of MERC-Tethering Proteins

We next investigated the effects of *OPA1* deletion in a mouse skeletal muscle-specific inducible knockout model (*OPA1* smKO) by TEM (Fig. 3A-D) and confocal microscopy (Fig. 3H-L). *OPA1* smKO resulted in a significant decrease in ER to mitochondrial distance (Fig. 3E). Both the mitochondrial surface area contacting the ER and the ER surface area contacting the mitochondria were increased in *OPA1* smKO animals (Fig. 3F, G). Confocal *in situ* PLA revealed increased MFN2–MFN1 (Fig. 3J: SV 6-7) and IP_3R3–VDAC interactions in each muscle fiber (Fig. 3M; SV 8–9), suggesting that OPA1 deficiency increases MERC proteins and MERC sites.

We previously reported that *OPA1* smKO animals exhibited ER stress activation and increased levels of the MERC protein MFN2 and its interacting partner MFN1 (Pereira et al., 2017). To determine whether other MERC protein levels were induced by OPA1-deficiency-associated mitochondrial stress, we used quantitative polymerase chain reaction (qPCR) to measure mRNA expression. In *OPA1* smKO samples MFN2, ER stress-related proteins (ATF4, BIP, CHOP and ATF6), and ternary Ca^{2+}-MERC complex members (IP_3R3, GRP75, and

VDAC3) were all increased (Fig. 3N). Four weeks after tamoxifen injections, mice were treated either with PBS or with the chemical ER chaperone tauroursodeoxycholic acid (TUDCA) for 4 weeks (12 weeks of age). TUDCA treatment attenuates ER stress activation in OPA1-deficient mouse muscles (Pereira et al., 2017; Tezze et al., 2017). Following TUDCA treatment, we observed decreased expression of Ca^{2+}-related MERC genes *VDAC3*, IP_3R3, and *GRP75* in 12-week-old *OPA1* smKO mice relative to untreated *OPA1* smKO mice (Figure 3O–Q). These results indicate that alleviation of ER stress by TUDCA reduced the expression of MERC genes related to Ca^{2+} transfer.

To further confirm increased expression of MERC-related proteins, we analyzed *OPA1* smKO samples by western blot (Fig. 3R). OPA1-deficient skeletal muscles from 40-week-old mice showed increased levels of BIP, PACS2, GRP75 and the OMM fusion proteins MFN2 and MFN1 (Fig. 3S). Thus, OPA1 deficiency, or the associated mitochondrial dysfunction (Pereira et al., 2021), induces the integrated stress response and expression levels of specific MERC-tethering proteins.

SBF-SEM Demonstrates Increased MERCs in *Opa1-like* KD in *Drosophila* Muscle, *OPA1* deficient Skeletal Muscle, and *OPA1* KO Primary Myotubes

Because TEM only captures structural MERC changes in two dimensions (2D), serial block facing-scanning electron microscopy (SBF-SEM) was used to assess MERC changes in a three-dimensional (3D) context. The apposition of the mitochondrial network and the ER depends on cellular metabolic transitions; therefore, we quantified the percentage of mitochondrion surface area covered by the ER and the percentage of the ER surface area covered by mitochondria in *Drosophila* muscle (Fig. 4A-D, SV10-SV11). The percentage coverage for

both mitochondria and ER significantly increased in the *Opa1-like* KD relative to the WT muscle (Fig. 4E, F, SV 10-11). Additionally, we used high-resolution 3D reconstructions to reconstruct ER and identify MERCs (SF 2A-B). Together, these results demonstrate that OPA1 deficiency increases MERC formation in *Drosophila* skeletal muscle.

3D reconstructions were also performed in murine control and *OPA1* deficient myotubes (Fig. 4G-L; SF2C-D) to study MERC formation *in vitro*. These studies revealed an increased percentage in the coverage of mitochondria by ER and an increased percentage in the coverage of ER by mitochondria in *OPA1* deficient myotubes (Fig. 4K, L, SV14-15).

We recapitulated these findings in mouse skeletal muscle using SBF-SEM (Fig. 4M-R, SV12-13, SF2E-F). Both mitochondrial and ER percent coverage increased significantly with OPA1 ablation (Fig. 4Q, R). These combined TEM and SBF-SEM results demonstrate that OPA1 ablation increased MERCs protein expression and tethering.

Gene Expression Profiles Associated with the Loss of *OPA1*

To fully evaluate the transcriptional adaptations to OPA1 deficiency and its relationship to MERCs formation in *Drosophila*, RNA sequencing (RNA-Seq) was performed. Ingenuity Pathway Analysis (IPA) of the RNA-seq data revealed that multiple ER stress and Ca^{2+} signaling genes were induced, whereas genes involved in mitochondrial function were repressed (Fig. 5A). This pattern was further substantiated by using canonical pathway analysis, which revealed eukaryotic initiation factor 2 (EIF2) signaling, an index of ER stress as being most highly induced, whereas oxidative phosphorylation and other mitochondrial processes related to mitochondrial dysfunction pathways were most repressed (Fig. 5B). IPA Upstream Regulator analysis revealed potential essential upstream signals that mediated changes in gene expression.

Significant activation of various known ER stress regulatory factors, the inactivation of Ca^{2+} signaling regulatory microRNAs, and both the activation and inhibition of mitochondrial dysfunction regulators were observed (Fig. 5C). The aggregated IPA canonical pathways are highly enriched in mitochondrial dysfunction, Ca^{2+} signaling, and ER stress-related pathways, indicating that OPA1 deficiency profoundly alters intracellular Ca^{2+} regulation (Fig. 5D, E). Notably, the IPA canonical pathway analysis identified ATF4 as an upstream regulator (Fig. 5C) and also revealed activation in mechanistic target of rapamycin (mTOR) complex 1 components, including RAPTOR, which are known to be involved in the regulation of the mitochondrial integrated stress response (Khan et al., 2017). To determine which gene expression pathways were altered by OPA1 loss, we generated a heat map of mTOR-targeted genes (SF 3). These results suggest that OPA1 deficiency activates mTOR signaling and pathways involved in ER stress activation, Ca^{2+} signaling, and mitochondrial dysfunction.

OPA1 Deficiency Alters Mitochondrial Ca^{2+} Uptake

The literature suggests that OPA1 plays a role in calcium oscillation and regulating MERC formation (Casellas□Díaz et al., 2021; De Brito and Scorrano, 2008; Han et al., 2021). Furthermore, our transcriptomics data reinforces the notion that Opa1 deletion impacts the expression of genes involved in Ca^{2+} homeostasis. We therefore sought to determine changes in Ca^{2+} dynamics in OPA1-deficient myotubes. Using caffeine (20 mM) as an agonist, we estimated the ability of mitochondria to take up Ca^{2+} released from the ER. First, we estimated mitochondrial Ca^{2+} concentration using mitopericam fluorescence from control and OPA1 KO primary myotubes (Fig. 6A). The area under the curve was decreased upon loss of OPA1, indicating that OPA1 loss reduces uptake of Ca^{2+} in the mitochondria (Fig. 6B). The peak amplitude for mitoPericam was decreased in OPA1 KO, which could be consistent with reduced

mitochondrial calcium uniporter (MCU) activity and activation rate upon loss of OPA1 (Fig. 6C). We, therefore, measured MCU levels in myoblasts, myotubes, and mouse skeletal muscle (SF 4). In all three models, loss of OPA1 increased MCU expression (SF 4B, E, H). To assess ER/SR calcium regulation, sarcoplasmic/endoplasmic reticulum Ca^{2+}-ATPase levels were measured and noted to be increased upon loss of OPA1 (SF4 C, F, I). Caffeine application is used to estimate SR Ca^{2+} (Figure 6D). OPA1 deficiency reduced the area under curve and peak amplitude (Figure 6E-F). When ER Ca^{2+} re-uptake by the ER was inhibited by thapsigargin (1 µM), both area under the curve and peak amplitude of cytosolic Ca^{2+} was decreased in OPA1-deficient cells following caffeine (20 mM) (Fig. 6G), indicating reduced ER Ca^{2+} stores (Fig. 6H-I). Taken together, OPA1 deficiency impairs mitochondrial Ca^{2+} homeostasis, despite induction of MCU and SERCA2 proteins. OPA1 loss activates an integrated stress response (Pereira et al., 2017). We sought to understand if deactivating the integrated stress response, by knocking out ATF4 (Pakos-Zebrucka et al., 2016), could restore Ca^{2+} homeostasis. We compared cytosolic Ca^{2+} measurements using Fura-2 from control, OPA1 KO and OPA1/ATF4 DKO primary myotubes in response to caffeine (Fig. 6J). Loss of OPA1 reduced the under the curve area (Fig. 6K) and the peak amplitude, indicating reduced Ca^{2+} release from the ER through Ryanodine receptors into the cytosol (Fig. 6L). Loss of ATF4 KO alone did not significantly change any calcium measures (Fig. 6J-L). However, when ATF4 and OPA1 were both knocked out, both the area under the curve and peak amplitude showed no significant difference between control and DKO mice, suggesting that ATF4 plays a role in regulating Ca^{2+} homeostasis in OPA1-deficient muscle cells (Fig. 6J-L).

ATF4 Mediates MERC Formation and Spacing in *OPA1*-deficient Skeletal Muscle

We hypothesized that ATF4 binds to the promoters of MERC genes and tested this by performing an *in-silico* study using publicly available CHiP-Seq data (Zou et al., 2022), which identified ATF4 binding to the promoters of GRP75 and VDAC3 (SF 5A-B). These data also suggest two potential ATF4 promoter binding sites in the IP_3R gene although these results are not as definitive (SF 5C). These observations support a potential role for ATF4 in the observed changes in MERC formation and protein expression under OPA1-deficient conditions (SF 4A-B). We sought to examine if distinct bioenergetic stress could trigger changes in MERC formation, by using oligomycin treatment to inhibit ATP synthase to induce mitochondrial stress in both human and mouse myotubes (SF 6A-C, G-I) (Guo et al., 2020; Mick et al., 2020). TEM analysis revealed no substantial changes in MERC length after 30 minutes of oligomycin treatment; however, significant increases in MERC lengths were observed after 8 hours of treatment in both cell types (SF 6D, J). No significant changes in MERC distance occurred after 30 minutes of treatment but decreased MERC distances were observed after 8 hours of treatment in both cell types (SF 6E, K). In human myotubes, ATF4 mRNA levels remained unchanged after 30 minutes of treatment but were significantly elevated after 8 hours of treatment (SF 6F). In mouse myotubes, ATF4 mRNA levels were significantly elevated after 30 minutes of treatment and persisted after 8 hours of treatment (SF 6L). Thus, bioenergetic stress induces ATF4 expression that correlates with stress-induced MERC changes.

To directly determine the relationship between ATF4 expression and MERC formation, studies were performed in ATF4 overexpression models. ATF4 overexpression in primary myotubes induced the expression of Ca^{2+}-related MERC proteins IP_3R3 and VDAC (Fig. 7A-D). MERC changes were examined by TEM in *ATF4* KO and OE skeletal muscle cells (Fig. 7E-J). Mean mitochondrial area was significantly decreased in both *OPA1* KO and *ATF4* KO muscle

cells, whereas the mean mitochondrial area was significantly increased in *ATF4* OE muscle cells (Fig. 7K). Double *OPA1* and *ATF4* KO and *OPA1* KO/*ATF4* OE resulted in non-significant reductions in the mitochondrial area relative to control skeletal muscle cells (Fig. 7K). *ATF4* KO significantly increased MERC distance, whereas *ATF4* OE significantly decreased MERC distance compared to the control (Fig. 7L). In *OPA1*/*ATF4* double-KO cells, a significant increase in MERC distance was observed, relative to control and OPA1 KO cells. These data suggest that ATF4 may regulate MERC formation and spacing in response to OPA1-deficiency.

We next sought to recapitulate these findings in *Drosophila* flight muscle, and SBF-SEM was used to further quantify ER and MERC lengths in *ATF4* KD and *ATF4* OE muscle (Fig. 7M-R, SV 16–18). A non-significant increase in ER length in *ATF4* KD muscle cells and an even greater increase in *ATF4* OE cells compared with control cells was observed (Fig. 7S). The ER volume did not significantly change in *ATF4* OE, but significantly increased in *ATF4* KD cells (Fig. 7T). The 3D MERC volume did not significantly change in *ATF4* KD cells but significantly increased in *ATF4* OE cells (Fig. 7U). TEM images of *ATF4* KD and OE in fly muscles were also analyzed (SF 7A-C). We observed an increase in MERC length in *ATF4* KD muscles and a slightly larger increase in the *ATF4* OE (SF 7D) muscles compared with control fly muscles. MERC distance increased in *ATF4* KD and decreased in *ATF4* OE muscles (SF 7E). Overexpression of *ATF4* similarly increased the MERC volume. Together, these data support the hypothesis that ATF4 may regulate MERC formation by inducing expression of MERC proteins and by decreasing the width of the MERC space and MERC length.

Discussion

MERCs mediate important intracellular communication processes between the ER and the mitochondria, including Ca^{2+} and lipid transfer, mitochondrial morphology regulation, and apoptosis. MERC defects are associated with the pathophysiology of various disorders including neurodegenerative illnesses, obesity and diabetes (Kim and Roy, 2020; Liao et al., 2017; Pereira et al., 2017; Tubbs et al., 2018; Verma et al., 2016). By studying the mechanisms that regulate MERC formation and maintenance, the roles of MERCs in cellular physiology and metabolism, are beginning to be elucidated. However, the relationship between mitochondrial dynamics, mitochondrial stress and MERCs have not yet been rigorously addressed. In the present study, we demonstrated that OPA1-deficiency increased the expression of multiple key MERC proteins, including MFN2, MFN1, PACS2, and BIP that paralleled bioenergetics defects. OPA1-deficiency also altered MERC tethering at the ultrastructural level and increased MERC volume and percent coverage in skeletal muscle, as determined by SBF-SEM. Importantly, we also elucidated that ATF4 might regulate MERC gene expression in response to mitochondrial stress, which could represent an initial compensatory mechanism that becomes persistent and ultimately maladaptive.

The reduction or loss of OPA1 expression results in increased expression of MFN2, a tethering MERC protein that regulates Ca^{2+} levels in the MERC space (Ainbinder et al., 2015), and of the ER stress protein ATF4 (De Brito and Scorrano, 2008; Naon et al., 2016; Pereira et al., 2017; Sood et al., 2014). MERC thickness should be precisely maintained to ensure normal Ca^{2+} transport, as an insufficient distance can result in steric hindrance among various components of the Ca^{2+} transporter machinery (Giacomello and Pellegrini, 2016). Ca^{2+} uptake between the ER and mitochondria is more likely to occur when the organelles are in close proximity, with an ideal distance ranging from 15–30 nm (Csordás et al., 2018; Giacomello and

Pellegrini, 2016; Thoudam et al., 2019). Reduced OPA1 expression decreased MERC distance, suggesting that OPA1 loss, induced structural changes in MERCs, which were correlated with an increase in the protein levels of IP_3R, GRP75, and VDAC3 in the MERC space. These proteins are crucial for Ca^{2+} transfer between the two organelles. Interestingly, despite this reduction in MERCs distance and increased protein levels of IP_3R, GRP75, and VDAC3, we confirmed prior results (Cartes-Saavedra et al., 2020) showing mitochondrial Ca^{2+} uptake was reduced in OPA1-deficient myotubes. The discrepancy between expression of proteins that promote mitochondrial Ca^{2+} uptake (including MCU), versus the measured reductions in SR and mitochondrial calcium content, underscore additional mechanisms that exist, by which OPA1 loss will impair cellular Ca^{2+} homeostasis. They also suggest that induction of the ATF4-dependent pathways identified, could represent an adaptive response. We validated previous results (Cretin et al., 2021; Parra et al., 2014) showing that loss of OPA1 increases mitochondrial fragmentation in concert with the induction of *DRP1*, a regulator of mitochondrial fission (Favaro et al., 2019; Möpert et al., 2009). Mitochondrial size is also known to influence calcium uptake (Golic et al., 2014; Handran et al., 1997; Kowaltowski et al., 2019), representing an additional mechanism by which OPA1 deficiency could impair intracellular calcium homeostasis.

Changes in MERC properties may also modulate ER to mitochondrial Ca^{2+} transfer, which serves an essential role in the regulation of mitochondrial energy metabolism, given that mitochondrial Ca^{2+} promotes oxidative phosphorylation (Bravo et al., 2011; Glancy and Balaban, 2012; Rieusset, 2018). Ca^{2+} concentrations regulate the activation of the TCA cycle, and increased Ca^{2+} levels in the mitochondrial matrix activate multiple enzymes involved in energy production (Carreras-Sureda et al., 2019; Denton et al., 1975; Glancy et al., 2013; Ivannikov and Macleod, 2013; Traaseth et al., 2004). Thus, the reduced intramitochondrial Ca^{2+} levels could

contribute to the bioenergetics impairment associated with OPA1 deficiency in addition to changes related to alterations in crista morphology. Altered MERC morphology in skeletal muscles following OPA1 loss could represent a compensatory mechanism to restore Ca^{2+} homeostasis (Cartes-Saavedra et al., 2020, 2021; Fülöp et al., 2011; Kushnareva et al., 2013). Similarly, IP_3R induction could represent an adaptive response. Sustained ER stress impairs mitochondrial metabolism, and the inhibition of IP_3R, a MERC component induced by OPA1-deficiency, can impair mitochondrial function and induce autophagy. Moreover, SERCA induction may attenuate ER stress and improve mitochondrial quality control (Tan et al., 2020), suggesting that the increased expression observed in the current study could also represent an adaptive response. We cannot exclude the possibility that the associated ATF4-dependent MERCs changes observed in response to OPA1 deficiency might be mechanistically linked to the impairment of mitochondrial and SR calcium homeostasis observed, despite increased expression of MERCs proteins and mitochondrial-ER tethering. Canonical pathway analysis of IPA data revealed induction of pathways enriched for ER stress and Ca^{2+} regulation. Notable pathways included two well defined calcium-dependent transcription factors; CREB and NFAT. These data support our observation that calcium, as a second messenger, is an important mediator of the cellular phenotype of OPA1 deficiency and could contribute to the transcriptional changes observed.

Changes in mitochondria–ER cross-talk accompany the early stages of ER stress, suggesting that exchange in metabolites between the mitochondria and ER will be altered in response to various cellular insults (Bravo et al., 2011). The ER-stress-associated protein IRE1α, which was induced in *Opa1-like* KD flies in our experiments, has non-canonical functions in MERC regulation, Ca^{2+} flux between the ER and mitochondria, and the regulation of

mitochondrial respiration, indicating a tight association between ER stress MERC formation and the regulation of mitochondrial metabolism (Carreras-Sureda et al., 2019). OPA1 deficiency induced ER stress-related proteins, including the transcription factor ATF4, leading us to hypothesize that ATF4 might regulate MERC gene expression. Our *in-silico* study confirmed that ATF4 likely binds to the promoters of MERC genes GRP75 and VDAC3, supporting the hypothesis that ATF4 induction following OPA1 deficiency may mediate changes in MERC protein expression and MERC formation.

ATF4 restoration of MERCs following OPA1 loss may occur in a mTOR-dependent manner (Park et al., 2017; Torrence et al., 2021). RNAseq data revealed that loss of OPA-1 induces mTOR, a known regulator of ER and mitochondrial stress responses in fly muscle (Figure 5; SF3). mTOR, which is implicated in the integrated stress response, has been shown to activate ATF4 (Quirós et al., 2017; Ryan et al., 2021). The mTORC2 protein complex is also localized to MERCs, where it interacts with IP_3R and GRP78. mTORC2 deficiency can disrupt MERC formation and impair SR Ca^{2+} uptake and increase intracellular Ca^{2+} (Betz et al., 2013). mTORC2 also modulates insulin signaling, and MERC integrity has been demonstrated to be necessary for insulin signaling in the liver and skeletal muscle (Rieusset, 2018; Theurey and Rieusset, 2017). ATF4 is also phosphorylated by mTOR (Mao and Zhang, 2018), thus it is likely that altered mTOR signaling could contribute to the changes in ATF4 signaling and Ca^{2+} homeostasis observed in OPA1 deficient cells.

In summary, using a model of OPA1-deficiency-induced mitochondrial and ER stress we identify a link between increased ATF4 protein levels and the regulation of MERC formation. OPA1-deficiency leads to complex compensatory mechanisms, including changes in MERC formation and structure and Ca^{2+} homeostasis. Our data suggest that OPA1 deficiency activates

mechanisms mediated at least in part by ATF4, that regulates ER-mitochondria coupling and calcium homeostasis in skeletal muscle cells.

Acknowledgements:

This work was supported by NIH grants R01HL108379 and R01DK092065 to E.D.A; Division of Intramural Research of the National Heart, Lung, and Blood Institute (NHLBI, 1ZIAHL006221 and the National Institute of Arthritis and Musculoskeletal and Skin Diseases (NIAMS) to B.G.; The United Negro College Fund/Bristol-Myers Squibb E.E. Just Faculty Fund, Burroughs Wellcome Fund Career Awards at the Scientific Interface Award, Burroughs Wellcome Fund Ad-hoc Award, National Institutes of Health Small Research Pilot Subaward to 5R25HL106365-12 from the National Institutes of Health PRIDE Program, DK020593, Vanderbilt Diabetes and Research Training Center for DRTC Alzheimer's Disease Pilot & Feasibility Program to A.H.J.; National Institute of Health (NIH) NIDDK T-32, number DK007563 entitled Multidisciplinary Training in Molecular Endocrinology to Z.V.; UNCF/BMS EE United Negro College Fund/Bristol-Myers Squibb E.E. Just Postgraduate Fellowship in the Life Sciences Fellowship to H.K.B.; NIH NIA RF1AG55549, NIH NINDS R01NS107265, RO1AG062135, AG59093, AG072899 to E.T.; and NSF grant MCB #2011577I and NIH T32 5T32GM133353 to S.A.M. Its contents are solely the responsibility of the authors

and do not necessarily represent the official view of the NIH. The funders had no role in study design, data collection and analysis, decision to publish, or preparation of the manuscript.

Competing interests:

The authors have no disclosures to report.

References:

Ainbinder, A., Boncompagni, S., Protasi, F., and Dirksen, R.T. (2015). Role of Mitofusin-2 in mitochondrial localization and calcium uptake in skeletal muscle. Cell Calcium *57*, 14–24. https://doi.org/10.1016/j.ceca.2014.11.002.

Betz, C., Stracka, D., Prescianotto-Baschong, C., Frieden, M., Demaurex, N., and Hall, M.N. (2013). Feature Article: mTOR complex 2-Akt signaling at mitochondria-associated endoplasmic reticulum membranes (MAM) regulates mitochondrial physiology. Proc Natl Acad Sci U S A *110*, 12526–12534. https://doi.org/10.1073/pnas.1302455110.

Bravo, R., Vicencio, J.M., Parra, V., Troncoso, R., Munoz, J.P., Bui, M., Quiroga, C., Rodriguez, A.E., Verdejo, H.E., Ferreira, J., et al. (2011). Increased ER-mitochondrial coupling promotes mitochondrial respiration and bioenergetics during early phases of ER stress. J Cell Sci *124*, 2143–2152. https://doi.org/10.1242/jcs.080762.

Carreras-Sureda, A., Jaña, F., Urra, H., Durand, S., Mortenson, D.E., Sagredo, A., Bustos, G., Hazari, Y., Ramos-Fernández, E., Sassano, M.L., et al. (2019). Non-canonical function of IRE1α determines mitochondria-associated endoplasmic reticulum composition to control calcium transfer and bioenergetics. Nat Cell Biol *21*, 755–767. https://doi.org/10.1038/s41556-019-0329-y.

Cartes-Saavedra, B., Arancibia, D., Burté, F., Sjoberg, M., Estela Andres, M., Yu-Wai-Man, P., Hajnoczky, G., and Eisner, V. (2020). OPA1 GTPase and GE Domain-Specific Mutations Differentially Alter Mitochondrial Fusion Dynamics and Calcium Homeostasis. Biophysical Journal *118*, 184a. https://doi.org/10.1016/j.bpj.2019.11.1125.

Cartes-Saavedra, B., Yu-Wai-Man, P., Hajnoczky, G., and Eisner, V. (2021). Mitochondrial Ca2+ Uptake in OPA1 Cells is Upregulated through Functional ER-Mitochondria Coupling. Biophysical Journal *120*, 348a–349a. https://doi.org/10.1016/j.bpj.2020.11.2167.

Cartes-Saavedra, B., Macuada, J., Lagos, D., Arancibia, D., Andrés, M.E., Yu-Wai-Man, P., Hajnóczky, G., and Eisner, V. (2022). OPA1 Modulates Mitochondrial Ca2+ Uptake Through ER-Mitochondria Coupling. Frontiers in Cell and Developmental Biology *9*. .

Casellas□Díaz, S., Larramona□Arcas, R., Riqué□Pujol, G., Tena□Morraja, P., Müller□Sánchez, C., Segarra□Mondejar, M., Gavaldà□Navarro, A., Villarroya, F., Reina, M.,

and Martínez□Estrada, O.M. (2021). Mfn2 localization in the ER is necessary for its bioenergetic function and neuritic development. EMBO Reports e51954. .

Cipolat, S., de Brito, O.M., Dal Zilio, B., and Scorrano, L. (2004). OPA1 requires mitofusin 1 to promote mitochondrial fusion. Proceedings of the National Academy of Sciences *101*, 15927–15932. https://doi.org/10.1073/pnas.0407043101.

Costa-Mattioli, M., and Walter, P. (2020). The integrated stress response: From mechanism to disease. Science *368*, eaat5314. https://doi.org/10.1126/science.aat5314.

Courson, J.A., Landry, P.T., Spehlmann, E., Lafontant, P., Patel, N., Rumbaut, R., and Burns, A. (2021). Serial Block-Face Scanning Electron Microscopy (SBF-SEM) of Biological Tissue Samples. Journal of Visualized Experiments: Jove.

Cretin, E., Lopes, P., Vimont, E., Tatsuta, T., Langer, T., Gazi, A., Sachse, M., Yu-Wai-Man, P., Reynier, P., and Wai, T. (2021). High-throughput screening identifies suppressors of mitochondrial fragmentation in OPA1 fibroblasts. EMBO Mol Med *13*, e13579. https://doi.org/10.15252/emmm.202013579.

Csordás, G., Weaver, D., and Hajnóczky, G. (2018). Endoplasmic Reticulum–Mitochondrial Contactology: Structure and Signaling Functions. Trends in Cell Biology *28*, 523–540. https://doi.org/10.1016/j.tcb.2018.02.009.

De Brito, O.M., and Scorrano, L. (2008). Mitofusin 2 tethers endoplasmic reticulum to mitochondria. Nature *456*, 605–610. .

Delprat, B., Rieusset, J., and Delettre, C. (2019). Defective Endoplasmic Reticulum–Mitochondria Connection Is a Hallmark of Wolfram Syndrome. Contact *2*, 251525641984740. https://doi.org/10.1177/2515256419847407.

Denton, R.M., Randle, P.J., Bridges, B.J., Cooper, R.H., Kerbey, A.L., Pask, H.T., Severson, D.L., Stansbie, D., and Whitehouse, S. (1975). Regulation of mammalian pyruvate dehydrogenase. Mol Cell Biochem *9*, 27–53. https://doi.org/10.1007/BF01731731.

Favaro, G., Romanello, V., Varanita, T., Desbats, M.A., Morbidoni, V., Tezze, C., Albiero, M., Canato, M., Gherardi, G., and De Stefani, D. (2019). DRP1-mediated mitochondrial shape controls calcium homeostasis and muscle mass. Nature Communications *10*, 1–17. .

Frezza, C., Cipolat, S., De Brito, O.M., Micaroni, M., Beznoussenko, G.V., Rudka, T., Bartoli, D., Polishuck, R.S., Danial, N.N., and De Strooper, B. (2006). OPA1 controls apoptotic cristae remodeling independently from mitochondrial fusion. Cell *126*, 177–189. .

Fülöp, L., Szanda, G., Enyedi, B., Várnai, P., and Spät, A. (2011). The Effect of OPA1 on Mitochondrial Ca2+ Signaling. PLoS ONE *6*, e25199. https://doi.org/10.1371/journal.pone.0025199.

Garza-Lopez, E., Vue, Z., Katti, P., Neikirk, K., Biete, M., Lam, J., Beasley, H.K., Marshall, A.G., Rodman, T.A., Christensen, T.A., et al. (2022). Protocols for Generating Surfaces and

Measuring 3D Organelle Morphology Using Amira. Cells *11*, 65. https://doi.org/10.3390/cells11010065.

Giacomello, M., and Pellegrini, L. (2016). The coming of age of the mitochondria–ER contact: a matter of thickness. Cell Death Differ *23*, 1417–1427. https://doi.org/10.1038/cdd.2016.52.

Glancy, B., and Balaban, R.S. (2012). Role of mitochondrial Ca2+ in the regulation of cellular energetics. Biochemistry *51*, 2959–2973. https://doi.org/10.1021/bi2018909.

Glancy, B., Willis, W.T., Chess, D.J., and Balaban, R.S. (2013). Effect of calcium on the oxidative phosphorylation cascade in skeletal muscle mitochondria. Biochemistry *52*, 2793–2809. https://doi.org/10.1021/bi3015983.

Golic, I., Velickovic, K., Markelic, M., Stancic, A., Jankovic, A., Vucetic, M., Otasevic, V., Buzadzic, B., Korac, B., and Korac, A. (2014). Calcium-induced alteration of mitochondrial morphology and mitochondrial-endoplasmic reticulum contacts in rat brown adipocytes. Eur J Histochem *58*, 2377. https://doi.org/10.4081/ejh.2014.2377.

Guo, X., Aviles, G., Liu, Y., Tian, R., Unger, B.A., Lin, Y.-H.T., Wiita, A.P., Xu, K., Correia, M.A., and Kampmann, M. (2020). Mitochondrial stress is relayed to the cytosol by an OMA1-DELE1-HRI pathway. Nature *579*, 427–432. https://doi.org/10.1038/s41586-020-2078-2.

Hall, D.D., Ponce, J.M., Chen, B., Spitler, K.M., Alexia, A., Oudit, G.Y., Song, L.-S., and Grueter, C.E. (2017). Ectopic expression of Cdk8 induces eccentric hypertrophy and heart failure. JCI Insight *2*, 92476. https://doi.org/10.1172/jci.insight.92476.

Han, S., Zhao, F., Hsia, J., Ma, X., Liu, Y., Torres, S., Fujioka, H., and Zhu, X. (2021). The role of Mfn2 in the structure and function of endoplasmic reticulum-mitochondrial tethering in vivo. J Cell Sci *134*, jcs253443. https://doi.org/10.1242/jcs.253443.

Handran, S.D., Werth, J.L., DeVivo, D.C., and Rothman, S.M. (1997). Mitochondrial morphology and intracellular calcium homeostasis in cytochrome oxidase-deficient human fibroblasts. Neurobiol Dis *3*, 287–298. https://doi.org/10.1006/nbdi.1996.0125.

Hartwick Bjorkman, S., and Oliveira Pereira, R. (2021). The Interplay Between Mitochondrial Reactive Oxygen Species, Endoplasmic Reticulum Stress, and Nrf2 Signaling in Cardiometabolic Health. Antioxidants & Redox Signaling ars.2020.8220. https://doi.org/10.1089/ars.2020.8220.

Hirabayashi, Y., Kwon, S.-K., Paek, H., Pernice, W.M., Paul, M.A., Lee, J., Erfani, P., Raczkowski, A., Petrey, D.S., Pon, L.A., et al. (2017). ER-mitochondria tethering by PDZD8 regulates Ca^{2+} dynamics in mammalian neurons. Science *358*, 623–630. https://doi.org/10.1126/science.aan6009.

Ivannikov, M.V., and Macleod, G.T. (2013). Mitochondrial free Ca^{2+} levels and their effects on energy metabolism in Drosophila motor nerve terminals. Biophys J *104*, 2353–2361. https://doi.org/10.1016/j.bpj.2013.03.064.

Kasai, S., Yamazaki, H., Tanji, K., Engler, M.J., Matsumiya, T., and Itoh, K. (2019). Role of the ISR-ATF4 pathway and its cross talk with Nrf2 in mitochondrial quality control. J. Clin. Biochem. Nutr. *64*, 1–12. https://doi.org/10.3164/jcbn.18-37.

Kim, D., and Roy, S. (2020). Effects of Diabetes on Mitochondrial Morphology and Its Implications in Diabetic Retinopathy. Invest Ophthalmol Vis Sci *61*, 10. https://doi.org/10.1167/iovs.61.10.10.

Kowaltowski, A.J., Menezes-Filho, S.L., Assali, E.A., Gonçalves, I.G., Cabral-Costa, J.V., Abreu, P., Miller, N., Nolasco, P., Laurindo, F.R.M., Bruni-Cardoso, A., et al. (2019). Mitochondrial morphology regulates organellar Ca2+ uptake and changes cellular Ca2+ homeostasis. FASEB J *33*, 13176–13188. https://doi.org/10.1096/fj.201901136R.

Kushnareva, Y.E., Gerencser, A.A., Bossy, B., Ju, W.-K., White, A.D., Waggoner, J., Ellisman, M.H., Perkins, G., and Bossy-Wetzel, E. (2013). Loss of OPA1 disturbs cellular calcium homeostasis and sensitizes for excitotoxicity. Cell Death Differ *20*, 353–365. https://doi.org/10.1038/cdd.2012.128.

Lam, J., Katti, P., Biete, M., Mungai, M., AshShareef, S., Neikirk, K., Garza Lopez, E., Vue, Z., Christensen, T.A., Beasley, H.K., et al. (2021). A Universal Approach to Analyzing Transmission Electron Microscopy with ImageJ. Cells *10*, 2177. https://doi.org/10.3390/cells10092177.

Liao, C., Ashley, N., Diot, A., Morten, K., Phadwal, K., Williams, A., Fearnley, I., Rosser, L., Lowndes, J., Fratter, C., et al. (2017). Dysregulated mitophagy and mitochondrial organization in optic atrophy due to OPA1 mutations. Neurology *88*, 131–142. https://doi.org/10.1212/WNL.0000000000003491.

Mao, Z., and Zhang, W. (2018). Role of mTOR in Glucose and Lipid Metabolism. International Journal of Molecular Sciences *19*, 2043. https://doi.org/10.3390/ijms19072043.

Mick, E., Titov, D.V., Skinner, O.S., Sharma, R., Jourdain, A.A., and Mootha, V.K. (2020). Distinct mitochondrial defects trigger the integrated stress response depending on the metabolic state of the cell. Elife *9*, e49178. https://doi.org/10.7554/eLife.49178.

Möpert, K., Hajek, P., Frank, S., Chen, C., Kaufmann, J., and Santel, A. (2009). Loss of Drp1 function alters OPA1 processing and changes mitochondrial membrane organization. Exp Cell Res *315*, 2165–2180. https://doi.org/10.1016/j.yexcr.2009.04.016.

Mustafi, D., Kikano, S., and Palczewski, K. (2014). Serial Block Face□Scanning Electron Microscopy: A Method to Study Retinal Degenerative Phenotypes. Current Protocols in Mouse Biology *4*, 197–204. .

Naon, D., Zaninello, M., Giacomello, M., Varanita, T., Grespi, F., Lakshminaranayan, S., Serafini, A., Semenzato, M., Herkenne, S., and Hernández-Alvarez, M.I. (2016). Critical reappraisal confirms that Mitofusin 2 is an endoplasmic reticulum–mitochondria tether. Proceedings of the National Academy of Sciences *113*, 11249–11254. .

Neikirk, K., Vue, Z., Katti, P., Shao, J., Christensen, T.A., Lopez, E.G., Marshall, A., Palavicino-Maggio, C., Ponce, J., and Alghanem, A. (2021). Systematic Transmission Electron Microscopy-Based Identification of Cellular Degradation Machinery. BioRxiv.

Pakos-Zebrucka, K., Koryga, I., Mnich, K., Ljujic, M., Samali, A., and Gorman, A.M. (2016). The integrated stress response. EMBO Rep *17*, 1374–1395. https://doi.org/10.15252/embr.201642195.

Park, Y., Reyna-Neyra, A., Philippe, L., and Thoreen, C.C. (2017). mTORC1 Balances Cellular Amino Acid Supply with Demand for Protein Synthesis through Post-transcriptional Control of ATF4. Cell Rep *19*, 1083–1090. https://doi.org/10.1016/j.celrep.2017.04.042.

Parra, V., Verdejo, H.E., Iglewski, M., Del Campo, A., Troncoso, R., Jones, D., Zhu, Y., Kuzmicic, J., Pennanen, C., and Lopez□Crisosto, C. (2014). Insulin stimulates mitochondrial fusion and function in cardiomyocytes via the Akt-mTOR-NFκB-Opa-1 signaling pathway. Diabetes *63*, 75–88. .

Patra, M., Mahata, S.K., Padhan, D.K., and Sen, M. (2016). CCN6 regulates mitochondrial function. Journal of Cell Science *129*, 2841–2851. https://doi.org/10.1242/jcs.186247.

Patten, D.A., Wong, J., Khacho, M., Soubannier, V., Mailloux, R.J., Pilon-Larose, K., MacLaurin, J.G., Park, D.S., McBride, H.M., Trinkle-Mulcahy, L., et al. (2014). OPA1-dependent cristae modulation is essential for cellular adaptation to metabolic demand. EMBO J *33*, 2676–2691. https://doi.org/10.15252/embj.201488349.

Pereira, R.O., Tadinada, S.M., Zasadny, F.M., Oliveira, K.J., Pires, K.M.P., Olvera, A., Jeffers, J., Souvenir, R., Mcglauflin, R., and Seei, A. (2017). OPA 1 deficiency promotes secretion of FGF 21 from muscle that prevents obesity and insulin resistance. The EMBO Journal *36*, 2126–2145. .

Pereira, R.O., Marti, A., Olvera, A.C., Tadinada, S.M., Bjorkman, S.H., Weatherford, E.T., Morgan, D.A., Westphal, M., Patel, P.H., and Kirby, A.K. (2021). OPA1 deletion in brown adipose tissue improves thermoregulation and systemic metabolism via FGF21. Elife *10*, e66519. .

Ponce, J.M., Coen, G., Spitler, K.M., Dragisic, N., Martins, I., Hinton, A., Mungai, M., Tadinada, S.M., Zhang, H., Oudit, G.Y., et al. (2020). Stress-Induced Cyclin C Translocation Regulates Cardiac Mitochondrial Dynamics. J Am Heart Assoc *9*, e014366. https://doi.org/10.1161/JAHA.119.014366.

Quirós, P.M., Prado, M.A., Zamboni, N., D'Amico, D., Williams, R.W., Finley, D., Gygi, S.P., and Auwerx, J. (2017). Multi-omics analysis identifies ATF4 as a key regulator of the mitochondrial stress response in mammals. J Cell Biol *216*, 2027–2045. https://doi.org/10.1083/jcb.201702058.

Rieusset, J. (2018). The role of endoplasmic reticulum-mitochondria contact sites in the control of glucose homeostasis: an update. Cell Death Dis *9*, 388. https://doi.org/10.1038/s41419-018-0416-1.

Romanello, V., and Sandri, M. (2015). Mitochondrial Quality Control and Muscle Mass Maintenance. Front Physiol *6*, 422. https://doi.org/10.3389/fphys.2015.00422.

Ryan, D.G., Yang, M., Prag, H.A., Blanco, G.R., Nikitopoulou, E., Segarra-Mondejar, M., Powell, C.A., Young, T., Burger, N., Miljkovic, J.L., et al. (2021). Disruption of the TCA cycle reveals an ATF4-dependent integration of redox and amino acid metabolism. Elife *10*, e72593. https://doi.org/10.7554/eLife.72593.

Sasaki, K., Uchiumi, T., Toshima, T., Yagi, M., Do, Y., Hirai, H., Igami, K., Gotoh, K., and Kang, D. (2020). Mitochondrial translation inhibition triggers ATF4 activation, leading to integrated stress response but not to mitochondrial unfolded protein response. Bioscience Reports *40*, BSR20201289. https://doi.org/10.1042/BSR20201289.

Scorrano, L., Ashiya, M., Buttle, K., Weiler, S., Oakes, S.A., Mannella, C.A., and Korsmeyer, S.J. (2002). A distinct pathway remodels mitochondrial cristae and mobilizes cytochrome c during apoptosis. Dev Cell *2*, 55–67. https://doi.org/10.1016/s1534-5807(01)00116-2.

Sood, A., Jeyaraju, D.V., Prudent, J., Caron, A., Lemieux, P., McBride, H.M., Laplante, M., Tóth, K., and Pellegrini, L. (2014). A Mitofusin-2–dependent inactivating cleavage of Opa1 links changes in mitochondria *cristae* and ER contacts in the postprandial liver. Proc. Natl. Acad. Sci. U.S.A. *111*, 16017–16022. https://doi.org/10.1073/pnas.1408061111.

Tan, Y., Mui, D., Toan, S., Zhu, P., Li, R., and Zhou, H. (2020). SERCA Overexpression Improves Mitochondrial Quality Control and Attenuates Cardiac Microvascular Ischemia-Reperfusion Injury. Mol Ther Nucleic Acids *22*, 696–707. https://doi.org/10.1016/j.omtn.2020.09.013.

Tezze, C., Romanello, V., Desbats, M.A., Fadini, G.P., Albiero, M., Favaro, G., Ciciliot, S., Soriano, M.E., Morbidoni, V., Cerqua, C., et al. (2017). Age-Associated Loss of OPA1 in Muscle Impacts Muscle Mass, Metabolic Homeostasis, Systemic Inflammation, and Epithelial Senescence. Cell Metab *25*, 1374-1389.e6. https://doi.org/10.1016/j.cmet.2017.04.021.

Theurey, P., and Rieusset, J. (2017). Mitochondria-Associated Membranes Response to Nutrient Availability and Role in Metabolic Diseases. Trends Endocrinol Metab *28*, 32–45. https://doi.org/10.1016/j.tem.2016.09.002.

Thoudam, T., Ha, C.-M., Leem, J., Chanda, D., Park, J.-S., Kim, H.-J., Jeon, J.-H., Choi, Y.-K., Liangpunsakul, S., Huh, Y.H., et al. (2019). PDK4 Augments ER-Mitochondria Contact to Dampen Skeletal Muscle Insulin Signaling During Obesity. Diabetes *68*, 571–586. https://doi.org/10.2337/db18-0363.

Torrence, M.E., MacArthur, M.R., Hosios, A.M., Valvezan, A.J., Asara, J.M., Mitchell, J.R., and Manning, B.D. (2021). The mTORC1-mediated activation of ATF4 promotes protein and glutathione synthesis downstream of growth signals. Elife *10*, e63326. https://doi.org/10.7554/eLife.63326.

Traaseth, N., Elfering, S., Solien, J., Haynes, V., and Giulivi, C. (2004). Role of calcium signaling in the activation of mitochondrial nitric oxide synthase and citric acid cycle. Biochim Biophys Acta *1658*, 64–71. https://doi.org/10.1016/j.bbabio.2004.04.015.

Tubbs, E., Theurey, P., Vial, G., Bendridi, N., Bravard, A., Chauvin, M.-A., Ji-Cao, J., Zoulim, F., Bartosch, B., and Ovize, M. (2014). Mitochondria-associated endoplasmic reticulum membrane (MAM) integrity is required for insulin signaling and is implicated in hepatic insulin resistance. Diabetes *63*, 3279–3294. .

Tubbs, E., Chanon, S., Robert, M., Bendridi, N., Bidaux, G., Chauvin, M.-A., Ji-Cao, J., Durand, C., Gauvrit-Ramette, D., Vidal, H., et al. (2018). Disruption of Mitochondria-Associated Endoplasmic Reticulum Membrane (MAM) Integrity Contributes to Muscle Insulin Resistance in Mice and Humans. Diabetes *67*, 636–650. https://doi.org/10.2337/db17-0316.

Varanita, T., Soriano, M.E., Romanello, V., Zaglia, T., Quintana-Cabrera, R., Semenzato, M., Menabò, R., Costa, V., Civiletto, G., and Pesce, P. (2015). The OPA1-dependent mitochondrial cristae remodeling pathway controls atrophic, apoptotic, and ischemic tissue damage. Cell Metabolism *21*, 834–844. .

Verma, A., Zhu, P., Prasad, T., Liang, Z., and Li, Q. (2016). Reduced Optic Atrophy 1 (OPA1) gene expression in diabetic retina- implication of mitochondrial dynamics in pathogenesis of diabetic retinopathy. Investigative Ophthalmology & Visual Science *57*, 5446. .

Vue, Z., Garza-Lopez, E., Neikirk, K., Vang, L., Beasley, H., Marshall, A.G., Murray, S.A., and Hinton Jr, A. (2022). Mouse Skeletal Muscle Decrease in the MICOS Complex and Altered Mitochondrial Networks with age. BioRxiv 2022–03. .

Zou, Z., Ohta, T., Miura, F., and Oki, S. (2022). ChIP-Atlas 2021 update: a data-mining suite for exploring epigenomic landscapes by fully integrating ChIP-seq, ATAC-seq and Bisulfite-seq data. Nucleic Acids Research *50*, W175–W182. https://doi.org/10.1093/nar/gkac199.

Figure Legend:

Figure 1. *Opa1-Like* knockdown (KD) in skeletal muscle alters mitochondrial morphology and mitochondrial-ER contact sites in *Drosophila*. (A). mRNA expression levels of mitochondria–endoplasmic reticulum (ER) contact (MERC) markers, IP_3R*3*, *GRP75* mRNA and *VDAC* and ER stress markers in *Opa1-like* KD compared with WT IFMs. (B-G). Adult myofibrils were stained with Phalloidin-FITC (F-actin) and mito-GFP (mitochondria). IFMs from WT flies revealed mitochondria with tubular morphology, whereas the *Opa1-like* KD flies showed clusters of

spherical mitochondria. (H). Mitochondria number (in three sarcomeres) in *Opa1-like* KD (n = 34) and WT (n = 32) IFMs. (I). Quantification of mitochondrial area (J). Mitochondrial aspect ratio (major axis/minor axis) in *OPA1-like KD* (n = 141) and WT (n = 105) IFMs. (K-N) Transmission electron microscopy (TEM) images showing cristae and mitochondrial morphology in WT and *Opa1-like* KD IFMs (n = 20). (O). Circularity index in *Opa1-like* KD IFMs relative to WT IFMs. (P). Quantification of mitochondrial area in *Opa1-like* KD and WT. (Q). Mitochondria number in *Opa1-like* KD and WT. (R). Cristae quality and abundance was assessed using the cristae score, on a scale from 0 (no sharply defined cristae) to 4 (many regular cristae). The average cristae score was significantly lower in *Opa1-like* KD than in WT. (S). Quantification of cristae area in *Opa1-like* KD and WT. (T). Cristae number in *Opa1-like* KO and WT. (U). Cristae volume in *Opa1-like* KD and WT. (V-Y). TEM images displaying MERCS in WT and *Opa1-like* KD IFMs (n = 20). (Z). Quantification of MERC lengths between *Opa1-like* KD and WT IFMs. (AA). quantification of MERC distance in *Opa1-like* KD and WT IFMs. (AB). Percentage of mitochondrial surface area in direct contact with the ER in *Opa1-like* KD and WT IFMs. (AC). Percentage of ER surface area in direct contact with mitochondria in *Opa1-like* KD and WT IFMs. *Significance was determined by two-tailed Student's t-test. * P<0.05, ** P<0.01, *** P<0.001, **** P < 0.0001.*

Figure 2. OPA1 knockout (*OPA1* KO) increases mitochondria–endoplasmic reticulum (ER) contact (MERC) formation in primary skeletal myoblasts and myotubes. (A) Representative immunoblot of ER stress proteins, ATF4 and BIP, and MERC-tethering proteins, MFN-2, and GRP-75, after infecting myotubes expressing $OPA1^{fl/fl}$ with Ad-GFP (WT) or Ad-Cre (KO). (B) Densitometric quantification demonstrating an increase in BIP, ATF4, MFN2, and GRP75 levels

in *OPA1* KO myotubes compared with WT, normalized to alpha tubulin. (C-H) *In situ* proximity ligation assay (PLA) showing MFN1–MFN2 interactions (red punctae) in *OPA1* KO and WT myoblasts (n = 10 cells, 3 independent experiments). Nuclei are labeled with 4′,6-diamidino-2-phenylindole (DAPI, blue). (I). Quantification showing increased MFN1–MFN2 puncta in *OPA1* KO compared with WT myoblasts. (J-V). Representative confocal images of *OPA1* KO and WT myoblasts (J-Q) and myotubes (R-W), with DAPI-labeled nuclei (blue) (J-N), mitotracker-labeled mitochondria (red) (K-O, R-U), GRP78 (L-P, S-V) showing the ER (green), and a composite image showing all channels (M-Q, T-W; n = 10 cells). (X) Co-localization (Pearson's correlation coefficient) is increased for ER and mitochondria in *OPA1* KO compared with WT myoblasts (Y, Z). Mander's overlap coefficient, demonstrating increased co-occurrence of ER and mitochondria in *OPA1* KO (Y) myoblasts (Z) and myotubes compared with WT. (AA-AD). Transmission electron microscopy (TEM) images of MERCs in primary *OPA1* KO and WT myotubes (Red arrows indicate mitochondria–ER interactions; n= 3 of 10 cells/experiment). Scale bar = 2 µm (2.5K magnification) and 500 nm (15K magnification). (AE) Quantification of MERC distance in *OPA1* KO and WT myotubes. (AF, AG). (AF) Percentage of mitochondrial surface area in direct contact with ER (AG) and percentage of ER surface area in direct contact with mitochondria in *OPA1* KO compared with WT myotubes. (AH). MERC area in *OPA1* KO compared with WT myotubes. (AI-AL). Cristae number (AI), area (AJ), score (AK) and volume (AL) in *OPA1* KO compared with WT. *Data are presented as the mean ± SEM. Significance was determined by Student's t-test. *P < 0.05, **P < 0.01, ***P < 0.001, **** P < 0.0001.*

Figure 3. OPA1 deficiency promotes mitochondria–endoplasmic reticulum (ER) contact (MERC) tethering in murine gastrocnemius skeletal muscle. (A-D). Transmission electron

microscopy (TEM) images showing MERCs in 20-week-old wild-type (WT) and *OPA1* skeletal muscle specific knockout (*OPA1* smKO) mice (n = 3). (E). MERC distance in *OPA1* smkO and WT controls. (F, G). Percentage coverage of (F) mitochondrial surface area and (G) ER surface area in *OPA1* smKO relative to WT. (H-M). *In situ* PLA visualization of MFN1–MNF2 (H-I, red punctae) and IP_3R3–VDAC interactions (K-L, red punctae) from 40-week-old WT and *OPA1* smKO mice. Quantification demonstrating (J) increased MFN1–MFN2 and (M) IP_3R3–VDAC interactions in *OPA1* smKO mice compared with WT (n = 3). (N). Quantification of mRNAs expressing reduced *OPA1*, ER stress genes *ATF4*, *BIP*, *CHOP*, and *ATF6*, MERC-tethering gene *MFN-2*, and calcium-related MERC genes IP_3R3, *Grp75*, and *VDAC3* in 40-week-old *OPA1* smKO compared with WT mice (n = 5). Data are expressed as fold changes vs. WT mice. (O–P). mRNA levels in 12□week□old *OPA1* smKO and WT mice 4 weeks after TUDCA treatment (n = 3). (O) IP_3R3 and (P) *GRP75* and (Q) *VDAC3* gene expression was significantly reduced in *OPA1*-smKO mice treated with TUDCA compared to without TUDCA. Data are presented as fold changes vs. WT mice. (R). Representative immunoblots showing MERC protein levels (normalized to GAPDH) in 40-week-old WT or *OPA1* smKO muscle (n = 6). (S) Densitometric quantification showing a significant increase in expression of BIP, GRP-75, MFN-2, and MFN-1 in *OPA1* smKO compared with WT mice. *Data are presented as the mean ± SEM. Significance was determined by Student's t-test. *P < 0.05, **P < 0.01, ***P < 0.001, **** P < 0.0001*.

Figure 4. OPA1 deficiency in skeletal muscle leads to the formation of mitochondrial–endoplasmic reticulum (ER) contacts (MERCs) in *Drosophila*, murine skeletal muscle and myotubes. The 3D distribution of single continuous and stationary mitochondria (purple, purple arrows) and ER (blue, blue arrows), reconstructed from serial block facing-scanning electron

microscopy (SBF-SEM) image stacks of *Drosophila* indirect flight muscle (IFM) fibers (A-D), *OPA1* KO primary myotubes (G-J), and *OPA1* skeletal muscle specific knockout (*OPA1* smKO) mouse muscle (M-P). (E, F). Percentage of ER surface area in contact with mitochondria (E) and percentage mitochondrial surface area in direct contact with ER (F) in *Opa1-like* KD compared with wild-type (WT) *Drosophila* skeletal muscle (SV1 [WT] SV2 [*Opa1-like* KD]). (K, L). Percentage of ER surface area in contact with mitochondria (K) and the percentage of mitochondria surface area in direct contact with ER (L) in *OPA1* smKO compared with WT myotubes. (Q, R). Percentage of ER surface area in contact with mitochondria (Q) and the percentage of mitochondria surface area in direct contact with ER (R) in *OPA1* KO compared with WT skeletal muscle. *Significance was determined using a non-parametric t-test. *P < 0.05, **P < 0.01, ***P < 0.001. SBF-SEM reconstructions from 7 to 23 fully constructed mitochondria, ER, or MERCs.*

Figure 5. Differential expression analysis of RNA-sequencing (RNA-seq) between WT and *Opa1-like* KD *Drosophila*. A. Scatter plot from RNA-seq comparing differentially expressed genes between WT and *Opa1-like* KD. Select upregulated (red) and downregulated genes (blue) are highlighted. (B). Ingenuity Pathway Analysis (IPA) signals for differentially expressed pathways implicated in mitochondria dysfunction (purple), ER stress (turquoise), and calcium signaling (orange). Negative Z-scores indicate inhibited pathways, and positive Z-scores represent activated pathways. (C). Select upstream regulators involved in mitochondria dysfunction (purple), ER stress (turquoise), and calcium signaling (orange), with activation Z-scores >2 or <−2. (D). IPA canonical pathways, with pathway names on the left and bars representing the Z-scores of corresponding pathways. (E). IPA canonical pathways, with names on the left and bars representing the −log (p-value)s of corresponding pathways.

Figure 6. (A). Mitochondria Ca^{2+} measurements after caffeine administration (20mM) using $_{mt}$pericam in control and OPA1 KO primary myotubes. (n=3). (B). Area under the curve for pericam showing decreased mitochondrial Ca^{2+} in OPA1 KO. (C). Quantification of peak amplitude pericam signal showing reduction in OPA1 primary myotubes. (D). Caffeine- induced (20mM) cytosol Ca^{2+} tracing measured by Fura-2 fluorescence in control and OPA1 KO primary myotubes(n=5). (E). Decreased area under the curve for cytosol Ca^{2+}in OPA1 KO myotubes. (F). Quantification of peak amplitude fura signal in OPA1 primary myotubes compared to control. (G). Cytosol Ca^{2+} levels by Fura recording in control and OPA- KO primary myotubes following treatment with Thapsigargin (Thaps) (1uM) and Caffeine (20mM) (n=5). (H). Area under the curve for Fura in OPA1 KO myotubes compared to control. (I). Quantification of peak amplitude Fura signal in OPA1 primary myotubes compared to control. (J). Cytosolic calcium tracing by fura in primary myotubes from OPA1 KO, ATF4 KO, and double KO (DKO) of OPA1 and ATF4. (K). Area under the curve decreases sequentially in ATF4 KO and OPA1 KO compared control. There is no significant change in DKO compared to control. (L). Peak amplitude quantification significantly decreases in KO of OPA1 compared to control.

Figure 7. ATF4 regulates mitochondria–endoplasmic reticulum (ER) contact (MERC) formation in OPA1-deficient muscle. (A) Representative immunoblot assessing ATF4, IP_3R3, and VDAC levels from Ad-GFP (WT) or *ATF4* overexpression (OE) mouse skeletal muscle myotubes (n=6) (B-D). Densitometric quantification demonstrating an increase in (B) ATF4, (C) IP_3R3 and (D) VDAC protein levels in *ATF4* OE compared with WT myotubes. (E-J) TEM panel comparing MERCs area in control, *OPA1* KO, *ATF4* KO, *ATF* OE, double *OPA1/ATF4* KO, and *OPA1*

KO/*ATF4* OE myotubes. Representative mitochondria are identified with purple arrows. (K) Mitochondrial area in *OPA1* KO, *ATF4* KO, ATF4 OE, *OPA1*/*ATF4* KO (DKO) and *OPA1* KO/*ATF4OE* relative to WT myotubes. (L) MERC distance in *OPA1* KO, *ATF4* KO, ATF4 OE, DKO and *OPA1* KO/*ATF4OE* relative to WT myotubes. (M-R). Individual electron micrograph of MERCs in control (M), *ATF4* KD (N), and *ATF4* OE myotubes and their serial block facing-scanning electron microscopy (SBF-SEM) 3D reconstructions (P-R), showing continuous, and stationary mitochondria (blue), nuclei (yellow), and ER (pink) in *Drosophila* flight muscle. Quantification of ER length (S), ER volume (T) and MERC volume (U) in control, ATF4 KD and ATF4 OE in *Drosophila* flight muscle. *Significance was determined by Student's t-test. *P < 0.05, **P < 0.01, ***P < 0.001, **** P < 0.0001.*

Supplementary Materials:

Supplemental Figure 1. Reduced pupal size and reduced mobility in *Opa1-like* knockdown (KD) (A). Decreased pupa mass of the *Opa1-like* KD compared with WT fly. (B). Fly steps per second were significantly decreased in *Opa1-like* KD compared with WT fly. (C). Three representative transmission electron microscopy (TEM) images of glycogen (small, black puncta) in WT and *Opa1-like* KD. (D). Glycogen levels in the *Opa1-like* KD flies compared with WT flies. *Data are presented as the mean ± SEM. Significance was determined using Student's t-test.* *P < 0.05, ****P < 0.0001.*

Supplemental Figure 2. Serial block facing-scanning electron microscopy (SBF-SEM) demonstrates that the loss of *OPA1* increases mitochondria–endoplasmic reticulum (ER) contacts

(MERCs). MERCs are shown in white in wild type (left) and *OPA1* KO in (A-B) *Drosophila* muscle, (C-D) primary skeletal muscle myotubes, and (E-F) murine muscle.

Supplemental Figure 3. OPA1 deficiency alters mechanistic target of rapamycin (mTOR) signaling gene expression pathways. (A) Heat map of the top 25 transcripts associated with the mTOR pathway, showing hierarchical clustering between two classes, *OPA1* KO and WT.

Supplemental Figure 4. Loss of OPA1 in Myotubes and Skeletal Muscle increases Mitochondrial Calcium Uniporter (MCU) and Sarcoplasmic/endoplasmic reticulum Ca^{2+}-ATPase (SERCA) Levels. (A). western blot showing (B) MCU and (C) SERCA levels following OPA1 KO in myoblasts. (D). Western blot showing (E) MCU and (F) SERCA levels following OPA1 KO in myotubes. (G). Western blot showing (H) MCU and (I) SERCA levels following OPA1 KO in mouse skeletal gastrocnemius muscle.

Supplemental Figure 5. *ATF4* binds to the promoter of the IP_3R-GRP75-VDAC MERC Complex. (A) *GRP75* promoter binding analysis in WT and ATF4 deficient cells, (B) *VDAC3* promoter binding analysis in WT and ATF4 deficient cells, and (C) IP_3R promoter binding analysis in WT and ATF4 deficient cells. Data obtained from a publicly available database: https://chip-atlas.org.

Supplemental Figure 6. Oligomycin induced stress increases MERC Formation in Human Primary Myotubes and Primary Murine Myotubes. Representative transmission electron microscopy (TEM) image of (A-C) human and (G-I) murine skeletal myotubes after oligomycin treatment for 0 h (control; A, G), 30 minutes (B, H), and 8h (C, I) following oligomycin [0.1 μg/ml] exposure. Blue arrow indicates MERC sites. (D) Analysis of MERC length in human skeletal muscle myotubes. (J) Analysis of MERC length in primary murine skeletal muscle myotubes. (E, K) Quantification of MERC distance at 0, 30 minutes and 8 h, oligomycin [0.1 μg/ml] exposure, in human skeletal myotubes (E) and primary murine skeletal myotubes (K). (F, L) *ATF4* mRNA levels in human myotubes (F) and mouse myotubes (L) at 0, 30 min and 8 h oligomycin [0.1 μg/ml] exposure.

Supplemental Figure 7. ATF4 alters mitochondrial–endoplasmic reticulum (ER) contact (MERC) spacing. (A-C). Transmission electron micrograph (TEM) images showing MERC spacing in (A) WT *Drosophila* skeletal muscle and after (B) *ATF4* KD and (C) *ATF4* OE. (D) Quantification of average MERC length in *ATF4* KD and *ATF4* OE compared with WT. (E) Quantification of MERC distance in *ATF4* KD and *ATF4* OE relative to WT.

Supplemental Table 1. qPCR Primers used for all studies involving mouse samples.

Supplemental Table 2. qPCR Primers used for all studies involving *Drosophila*.

Supplemental Videos 1–3. Loss of *Opa1-like* in *Drosophila* skeletal muscle decreases muscle movement. Live videos of fly movement for WT (Video 1) and *Opa1-like* KD (Video 2 and 3) flies.

Supplementary Videos 4–5. Representative 360° rotational view of confocal images in primary myoblasts after *OPA1* knockdown. Nuclei are labeled blue and MFN2–MFN1 interactions are labeled red. Supplemental Video 4 shows $OPA1^{fl/fl}$ while Supplemental Video 5 shows $OPA-1^{fl/fl}Cre$.

Supplementary Videos 6-9. Representative 360° rotational views of confocal images of mouse skeletal muscle. Muscle fibers are labeled gray and nuclei are labeled blue. Protein antibody interactions, MFN1–MFN2 and IP_3R3–VDAC interactions, are labeled in red. MFN1–MFN2 interactions are shown in WT (Video 6) and OPA1 smKO (Video 7). IP_3R3–VDAC interactions are shown in WT (Video 8) and OPA1 smKO (Video 9).

Supplemental Videos 10-11. Representative 360° rotational view of mitochondrial–endoplasmic reticulum (ER) contacts (MERCs) in mouse skeletal tissue as WT (Video 10) and after *OPA1* knockdown (Video 11), captured using serial block facing-scanning electron microscopy (SBF-SEM). Mitochondria are labeled blue, and ER is labeled pink.

Supplemental Videos 12–13. Representative 360° rotational view of mitochondria–endoplasmic reticulum (ER) contacts (MERCs) in primary myotubes as WT (Video 12) and after *OPA1*

knockdown (Video 13), captured with serial block facing-scanning electron microscopy (SBF-SEM). Mitochondria are labeled blue, and ER are labeled pink.

Supplemental Videos 14–15. Representative 360° rotational view of mitochondria–endoplasmic reticulum (ER) contacts (MERCs) in WT (Video 14) *Drosophila* and after *Opa1-like* knockdown (Video 15), captured with serial block facing-scanning electron microscopy (SBF-SEM). Mitochondria are labeled blue, and ER are labeled pink.

Supplemental Videos 16–18. Representative 360° rotational view of mitochondria–endoplasmic reticulum (ER) contacts (MERCs) in skeletal muscle from control (Video 16), *ATF4* KO (Video 17), and *ATF4* overexpression (Video 18), captured with serial block facing-scanning electron microscopy (SBF-SEM). Mitochondria are labeled blue, ER is labeled pink, and the nucleus is labeled yellow.

A

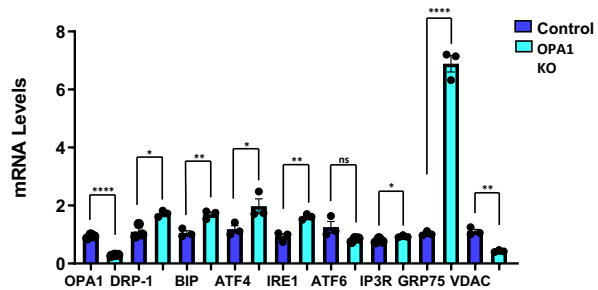
mRNA Levels
Control
OPA1 KO
OPA1
DRP-1
BIP
ATF4
IRE1
ATF6
IP3R
GRP75
VDAC

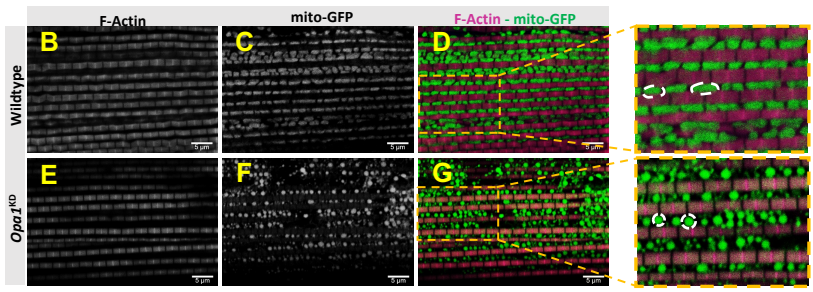
F-Actin
mito-GFP
F-Actin - mito-GFP
Wildtype
Opa1KD
B
C
D
E
F
G

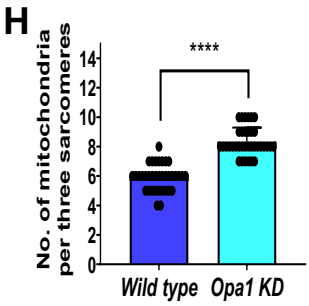
H
No. of mitochondria per three sarcomeres
Wild type
Opa1 KD

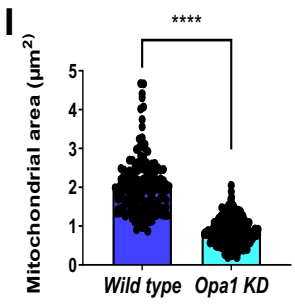
I
Mitochondrial area (μm²)
Wild type
Opa1 KD

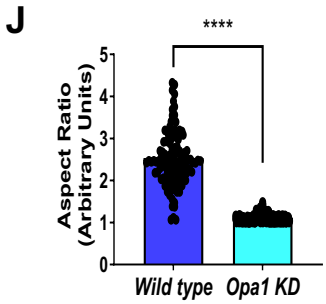
J
Aspect Ratio (Arbitrary Units)
Wild type
Opa1 KD

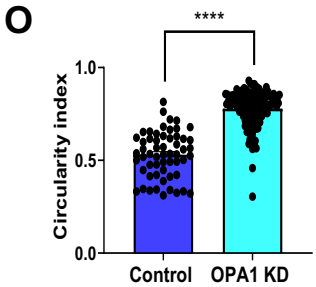
O
Circularity index
Control
OPA1 KD

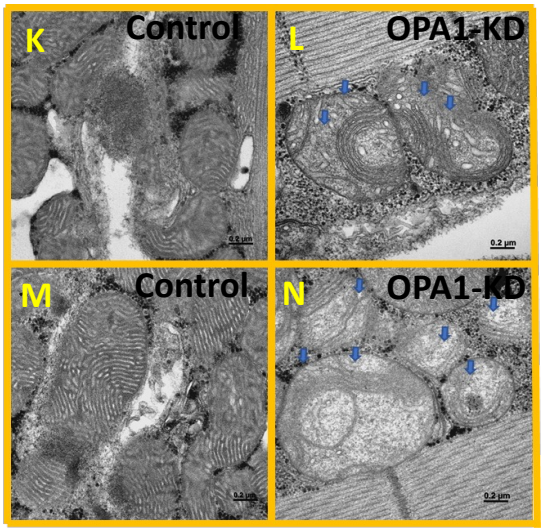
K
Control
L
OPA1-KD
M
Control
N
OPA1-KD

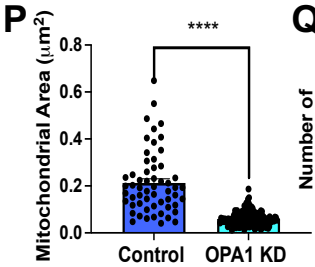
P
Mitochondrial Area (μm²)
Control
OPA1 KD

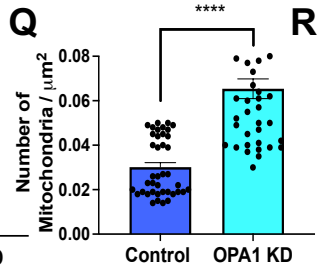
Q
Number of Mitochondria / μm²
Control
OPA1 KD

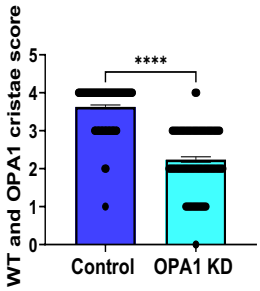
R
WT and OPA1 cristae score
Control
OPA1 KD

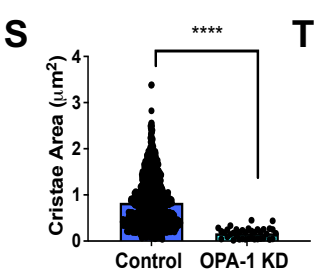
S
Cristae Area (μm²)
Control
OPA-1 KD

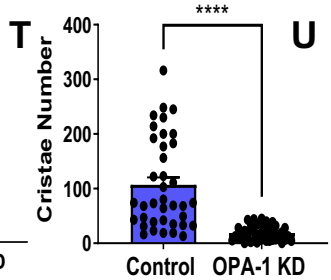
T
Cristae Number
Control
OPA-1 KD

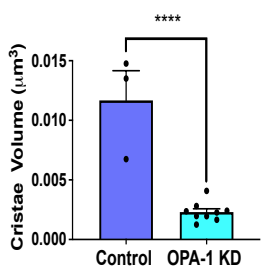
U
Cristae Volume (μm³)
Control
OPA-1 KD

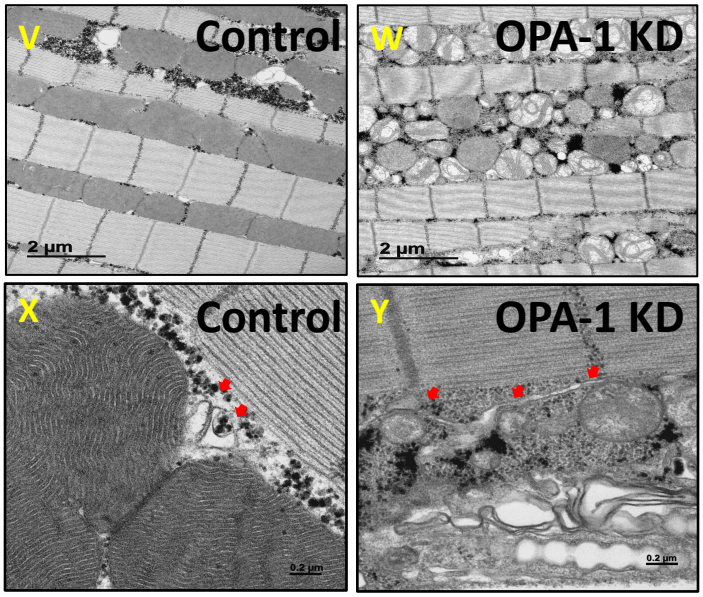
V
Control
W
OPA-1 KD
2 μm
2 μm
X
Control
Y
OPA-1 KD

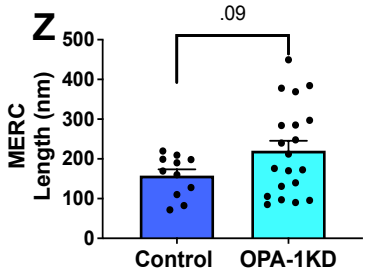
Z
.09
MERC Length (nm)
Control
OPA-1KD

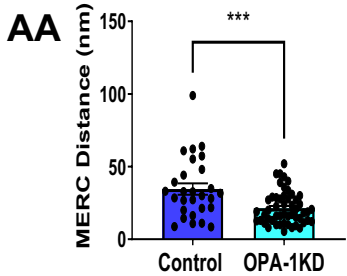
AA
MERC Distance (nm)
Control
OPA-1KD

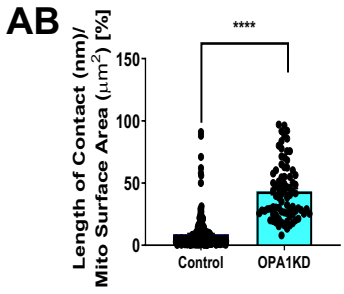
AB
Length of Contact (nm)/ Mito Surface Area (μm²) [%]
Control
OPA1KD

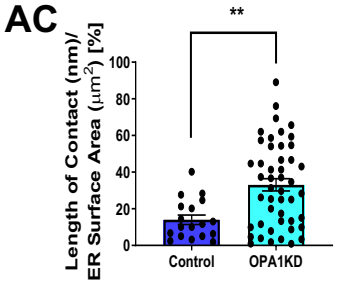
AC
Length of Contact (nm)/ ER Surface Area (μm²) [%]
Control
OPA1KD

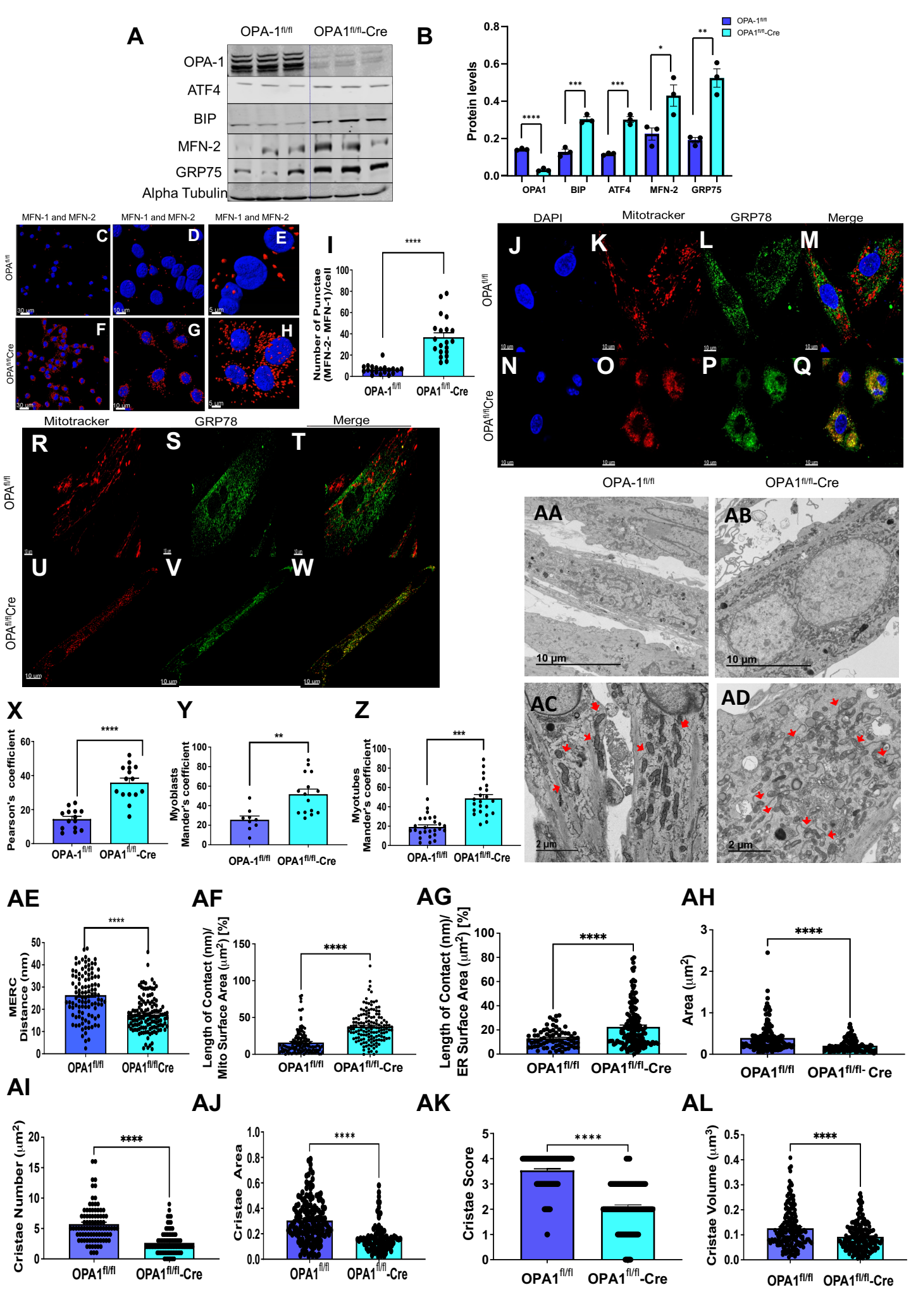
A
OPA-1fl/fl
OPA1fl/fl-Cre
OPA-1
ATF4
BIP
MFN-2
GRP75
Alpha Tubulin
B
Protein levels
OPA1
BIP
ATF4
MFN-2
GRP75
MFN-1 and MFN-2
OPAfl/fl
OPAfl/flCre
Number of Punctae (MFN-2- MFN-1)/cell
DAPI
Mitotracker
GRP78
Merge
Pearson's coefficient
Myoblasts Mander's coefficient
Myotubes Mander's coefficient
MERC Distance (nm)
Length of Contact (nm)/ Mito Surface Area (µm2) [%]
Length of Contact (nm)/ ER Surface Area (µm2) [%]
Area (µm2)
Cristae Number (µm2)
Cristae Area
Cristae Score
Cristae Volume (µm3)

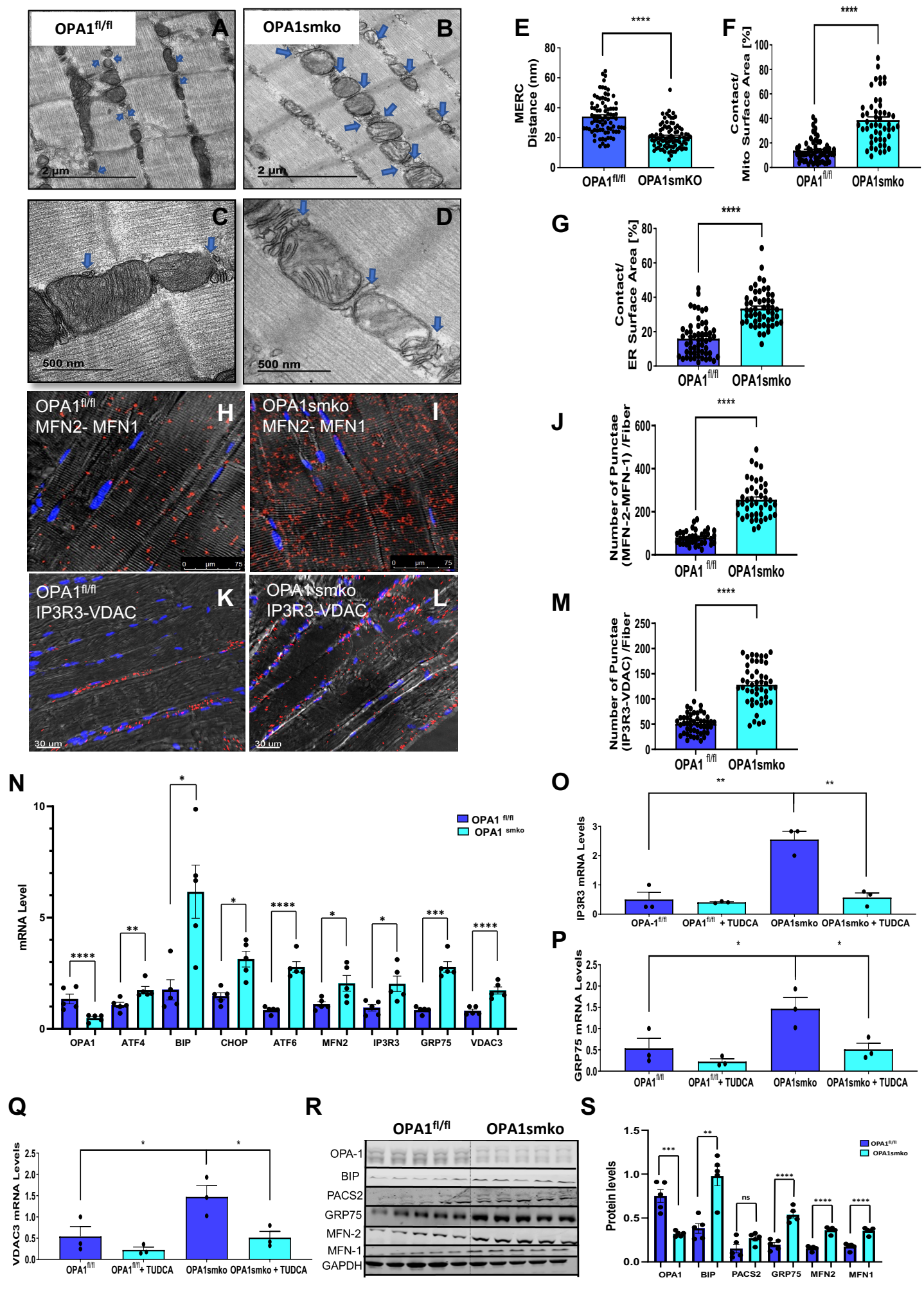
OPA1fl/fl
A
2 µm
OPA1smko
B
2 µm
C
500 nm
D
500 nm
OPA1fl/fl
MFN2- MFN1
H
OPA1smko
MFN2- MFN1
I
OPA1fl/fl
IP3R3-VDAC
K
OPA1smko
IP3R3-VDAC
L
30 um
30 um
E
MERC Distance (nm)
OPA1fl/fl
OPA1smKO
F
Contact/ Mito Surface Area [%]
OPA1fl/fl
OPA1smko
G
Contact/ ER Surface Area [%]
OPA1fl/fl
OPA1smko
J
Number of Punctae (MFN-2-MFN-1) /Fiber
OPA1fl/fl
OPA1smko
M
Number of Punctae (IP3R3-VDAC) /Fiber
OPA1fl/fl
OPA1smko
N
mRNA Level
OPA1fl/fl
OPA1smko
OPA1
ATF4
BIP
CHOP
ATF6
MFN2
IP3R3
GRP75
VDAC3
O
IP3R3 mRNA Levels
OPA-1fl/fl
OPA1fl/fl + TUDCA
OPA1smko
OPA1smko + TUDCA
P
GRP75 mRNA Levels
OPA1fl/fl
OPA1fl/fl + TUDCA
OPA1smko
OPA1smko + TUDCA
Q
VDAC3 mRNA Levels
OPA1fl/fl
OPA1fl/fl + TUDCA
OPA1smko
OPA1smko + TUDCA
R
OPA1fl/fl
OPA1smko
OPA-1
BIP
PACS2
GRP75
MFN-2
MFN-1
GAPDH
S
Protein levels
OPA1fl/fl
OPA1smko
OPA1
BIP
PACS2
GRP75
MFN2
MFN1

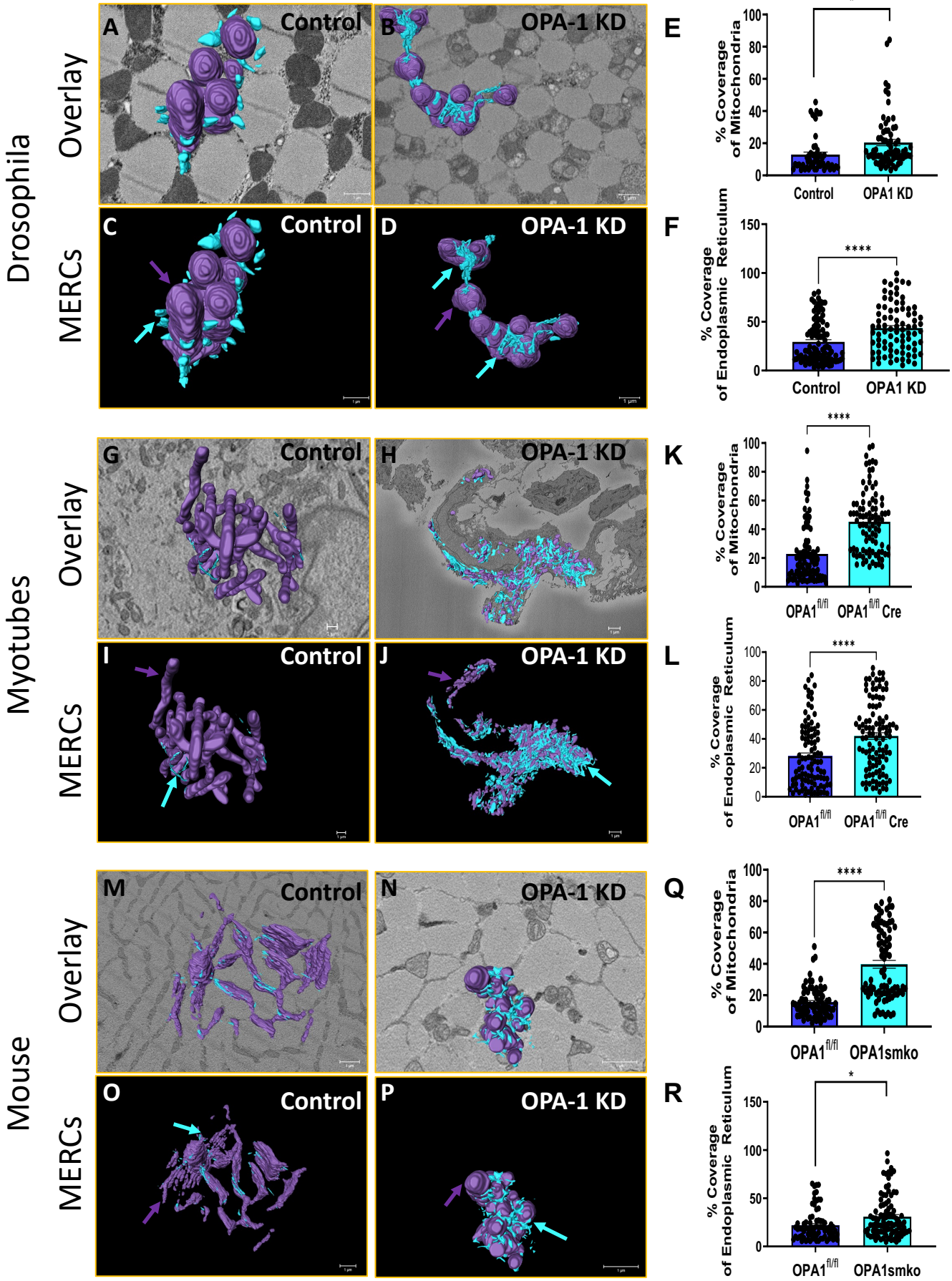
Drosophila
Overlay
MERCs
A
Control
B
OPA-1 KD
C
Control
D
OPA-1 KD
E
% Coverage of Mitochondria
Control
OPA1 KD
F
% Coverage of Endoplasmic Reticulum
Control
OPA1 KD
Myotubes
Overlay
MERCs
G
Control
H
OPA-1 KD
I
Control
J
OPA-1 KD
K
% Coverage of Mitochondria
OPA1fl/fl
OPA1fl/fl Cre
L
% Coverage of Endoplasmic Reticulum
OPA1fl/fl
OPA1fl/fl Cre
Mouse
Overlay
MERCs
M
Control
N
OPA-1 KD
O
Control
P
OPA-1 KD
Q
% Coverage of Mitochondria
OPA1fl/fl
OPA1smko
R
% Coverage of Endoplasmic Reticulum
OPA1fl/fl
OPA1smko

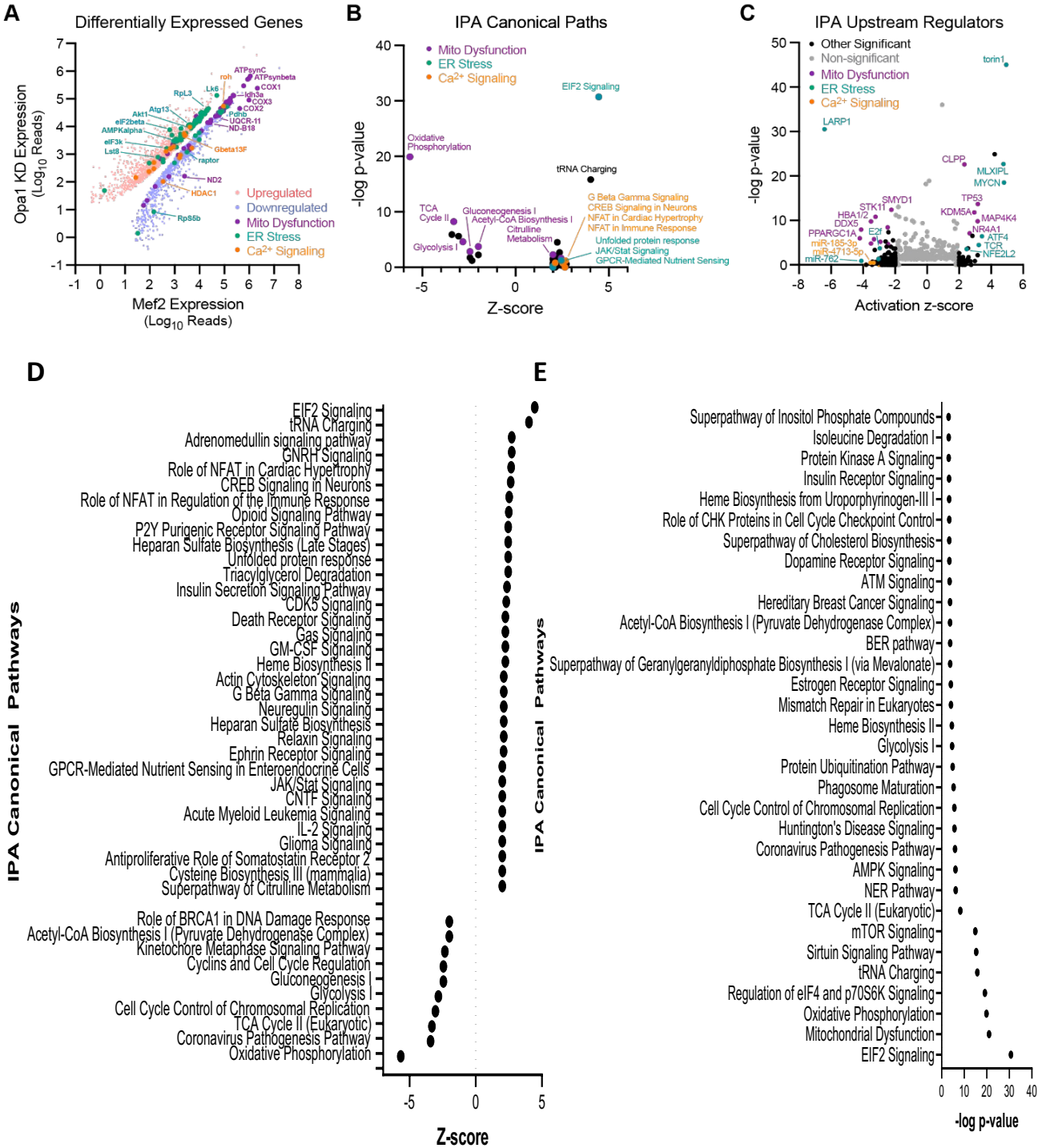
A
Differentially Expressed Genes
Opa1 KD Expression (Log10 Reads)
Mef2 Expression (Log10 Reads)
ATPsynC
ATPsynbeta
roh
COX1
Lk6
RpL3
Ldh3a
COX3
COX2
Atg13
Akt1
Pdhb
eIF2beta
UQCR-11
AMPKalpha
ND-B18
eIF3k
Lst8
Gbeta13F
raptor
ND2
HDAC1
Rps5b
Upregulated
Downregulated
Mito Dysfunction
ER Stress
Ca2+ Signaling
B
IPA Canonical Paths
-log p-value
Z-score
Mito Dysfunction
ER Stress
Ca2+ Signaling
EIF2 Signaling
Oxidative Phosphorylation
tRNA Charging
G Beta Gamma Signaling
CREB Signaling in Neurons
NFAT in Cardiac Hypertrophy
NFAT in Immune Response
Unfolded protein response
JAK/Stat Signaling
GPCR-Mediated Nutrient Sensing
TCA Cycle II
Gluconeogenesis I
Acetyl-CoA Biosynthesis I
Citrulline Metabolism
Glycolysis I
C
IPA Upstream Regulators
-log p-value
Activation z-score
Other Significant
Non-significant
Mito Dysfunction
ER Stress
Ca2+ Signaling
torin1
LARP1
CLPP
MLXIPL
MYCN
SMYD1
TP53
STK11
KDM5A
HBA1/2
MAP4K4
DDX5
NR4A1
PPARGC1A
E2f
ATF4
miR-185-3p
TCR
miR-4713-5p
NFE2L2
miR-762
D
IPA Canonical Pathways
Z-score
EIF2 Signaling
tRNA Charging
Adrenomedullin signaling pathway
GNRH Signaling
Role of NFAT in Cardiac Hypertrophy
CREB Signaling in Neurons
Role of NFAT in Regulation of the Immune Response
Opioid Signaling Pathway
P2Y Purigenic Receptor Signaling Pathway
Heparan Sulfate Biosynthesis (Late Stages)
Unfolded protein response
Triacylglycerol Degradation
Insulin Secretion Signaling Pathway
CDK5 Signaling
Death Receptor Signaling
Gas Signaling
GM-CSF Signaling
Heme Biosynthesis II
Actin Cytoskeleton Signaling
G Beta Gamma Signaling
Neuregulin Signaling
Heparan Sulfate Biosynthesis
Relaxin Signaling
Ephrin Receptor Signaling
GPCR-Mediated Nutrient Sensing in Enteroendocrine Cells
JAK/Stat Signaling
CNTF Signaling
Acute Myeloid Leukemia Signaling
IL-2 Signaling
Glioma Signaling
Antiproliferative Role of Somatostatin Receptor 2
Cysteine Biosynthesis III (mammalia)
Superpathway of Citrulline Metabolism
Role of BRCA1 in DNA Damage Response
Acetyl-CoA Biosynthesis I (Pyruvate Dehydrogenase Complex)
Kinetochore Metaphase Signaling Pathway
Cyclins and Cell Cycle Regulation
Gluconeogenesis I
Glycolysis I
Cell Cycle Control of Chromosomal Replication
TCA Cycle II (Eukaryotic)
Coronavirus Pathogenesis Pathway
Oxidative Phosphorylation
E
IPA Canonical Pathways
-log p-value
Superpathway of Inositol Phosphate Compounds
Isoleucine Degradation I
Protein Kinase A Signaling
Insulin Receptor Signaling
Heme Biosynthesis from Uroporphyrinogen-III I
Role of CHK Proteins in Cell Cycle Checkpoint Control
Superpathway of Cholesterol Biosynthesis
Dopamine Receptor Signaling
ATM Signaling
Hereditary Breast Cancer Signaling
Acetyl-CoA Biosynthesis I (Pyruvate Dehydrogenase Complex)
BER pathway
Superpathway of Geranylgeranyldiphosphate Biosynthesis I (via Mevalonate)
Estrogen Receptor Signaling
Mismatch Repair in Eukaryotes
Heme Biosynthesis II
Glycolysis I
Protein Ubiquitination Pathway
Phagosome Maturation
Cell Cycle Control of Chromosomal Replication
Huntington's Disease Signaling
Coronavirus Pathogenesis Pathway
AMPK Signaling
NER Pathway
TCA Cycle II (Eukaryotic)
mTOR Signaling
Sirtuin Signaling Pathway
tRNA Charging
Regulation of eIF4 and p70S6K Signaling
Oxidative Phosphorylation
Mitochondrial Dysfunction
EIF2 Signaling

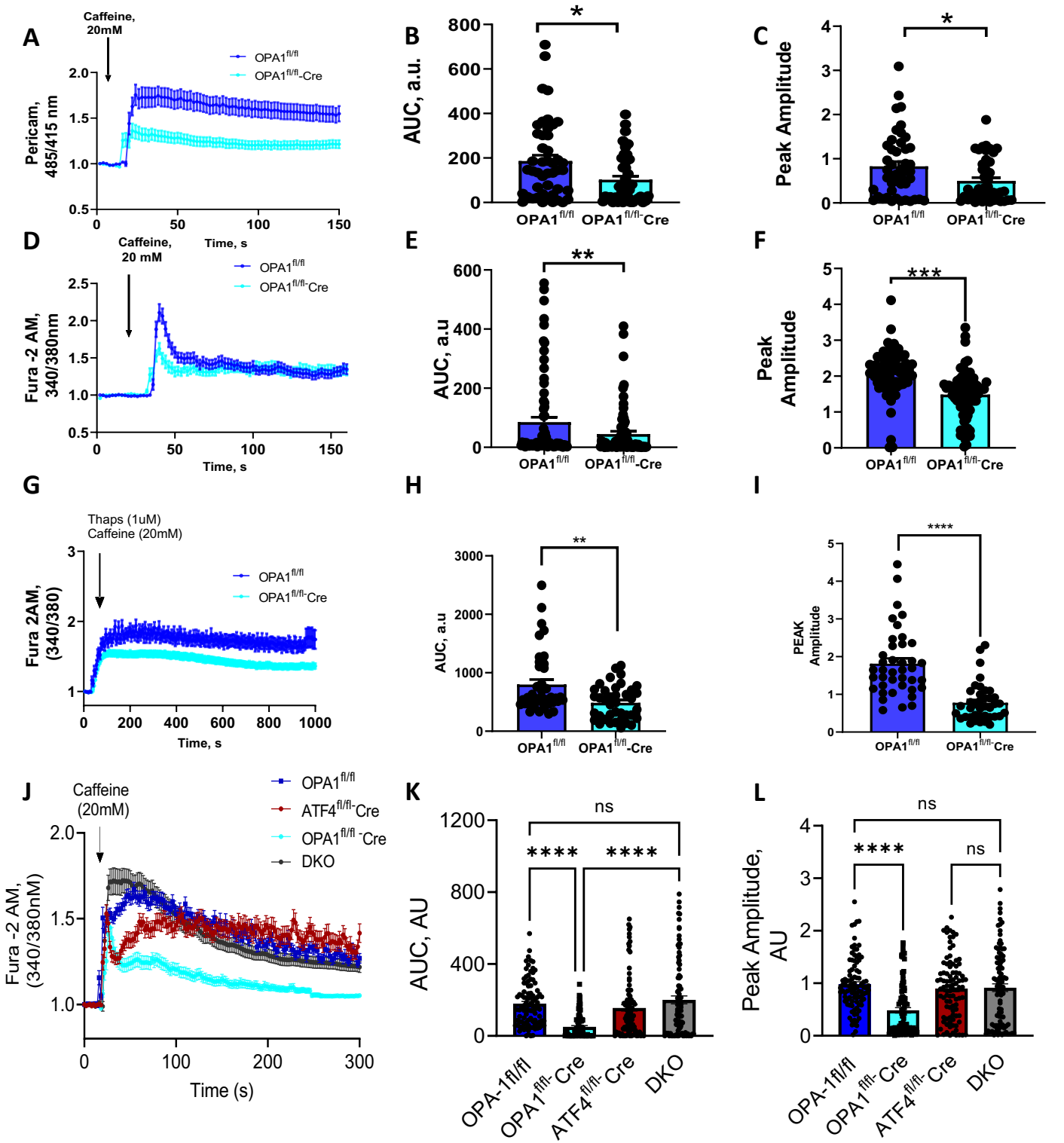
A
Caffeine, 20mM
OPA1fl/fl
OPA1fl/fl-Cre
Pericam, 485/415 nm
Time, s
B
AUC, a.u.
*
OPA1fl/fl
OPA1fl/fl-Cre
C
Peak Amplitude
*
D
Caffeine, 20 mM
Fura -2 AM, 340/380nm
E
AUC, a.u
**
F
Peak Amplitude
***
G
Thaps (1uM)
Caffeine (20mM)
Fura 2AM, (340/380)
H
AUC, a.u
**
I
PEAK Amplitude
****
J
Caffeine (20mM)
ATF4fl/fl-Cre
OPA1fl/fl -Cre
DKO
Fura -2 AM, (340/380nM)
Time (s)
K
AUC, AU
ns
****
****
OPA-1fl/fl
OPA1fl/fl-Cre
ATF4fl/fl-Cre
DKO
L
Peak Amplitude, AU
ns
****
ns

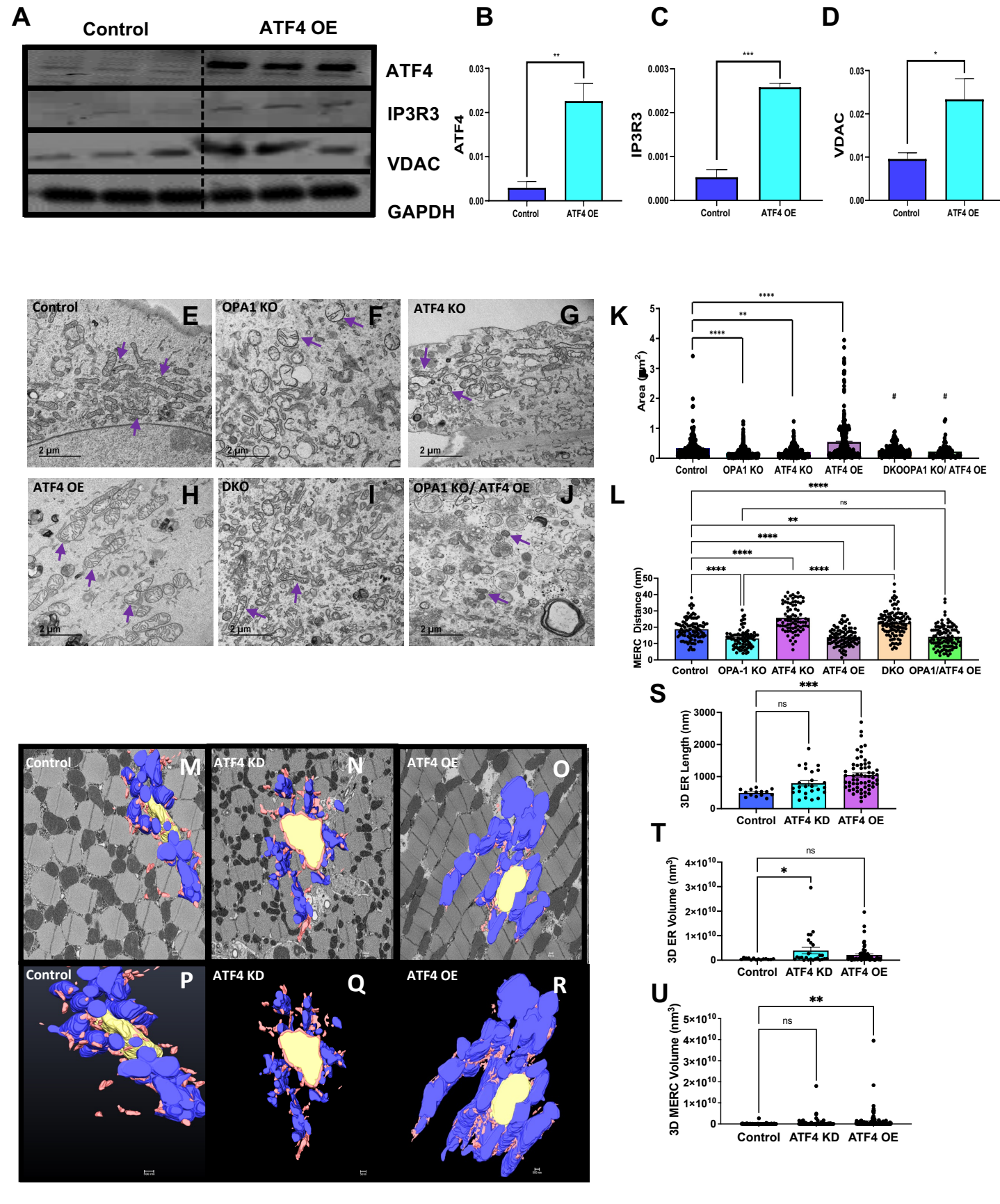
A
Control
ATF4 OE
ATF4
IP3R3
VDAC
GAPDH
B
ATF4
Control
ATF4 OE
C
IP3R3
D
VDAC
E
Control
F
OPA1 KO
G
ATF4 KO
H
ATF4 OE
I
DKO
J
OPA1 KO/ ATF4 OE
2 µm
K
Area (µm²)
Control
OPA1 KO
ATF4 KO
ATF4 OE
DKO
OPA1 KO/ ATF4 OE
L
MERC Distance (nm)
Control
OPA-1 KO
ATF4 KO
ATF4 OE
DKO
OPA1/ATF4 OE
M
Control
N
ATF4 KD
O
ATF4 OE
P
Control
Q
ATF4 KD
R
ATF4 OE
S
3D ER Length (nm)
Control
ATF4 KD
ATF4 OE
T
3D ER Volume (nm³)
Control
ATF4 KD
ATF4 OE
U
3D MERC Volume (nm³)
Control
ATF4 KD
ATF4 OE